Quantum-enhanced sensing and topological matter with ultracold dysprosium atoms

Sylvain Nascimbene

HABILITATION À DIRIGER DES RECHERCHES

Université de recherche Paris Sciences & Lettres
PSL Research University

préparée à l'École normale supérieure

Mémoire de synthèse et projet scientifique

Quantum-enhanced sensing and topological matter with ultracold dysprosium atoms

École doctorale n°564 Physique en Ile de France
Spécialité: Physique Atomique et Moléculaire Optique

Soutenue par

Sylvain Nascimbene

le 10 septembre 2020

Composition du Jury :

Mme Jacqueline Bloch
CNRS - C2N - Université Paris Saclay
Présidente du jury

M. Frédéric Chevy
École Normale Supérieure, Paris
Correspondant

M. Tilman Esslinger
ETH Zurich
Rapporteur

M. Bruno Laburthe-Tolra
CNRS - LPL - Université Paris 13
Rapporteur

M. Wilhelm Zwerger
Technische Universität, Munich
Rapporteur

ENS | PSL RESEARCH UNIVERSITY PARIS

Contents

Remerciements

Le travail présenté dans ce mémoire a été effectué au Laboratoire Kastler Brossel, à l'Ecole Normale Supérieure et au Collège de France. Je tiens à souligner la qualité de l'environnement scientifique de ces institutions. Ces lieux témoignent toujours des travaux d'éminents membres du laboratoire, qui ont permis l'essor du domaine des atomes froids au niveau mondial. Mon travail s'appuie évidemment sur cet héritage.

Je souhaite exprimer ma gratitude à Jean Dalibard, qui dirige notre équipe de recherche sur la condensation de Bose-Einstein. Le projet d'étude du dysprosium ultrafroid a été motivé par nos réflexions communes sur les possibilités de réalisation de champs de jauge dans les gaz atomiques. Plus généralement, les discussions scientifiques avec Jean sont extrêmement stimulantes et motivantes pour l'ensemble du groupe. Au delà de ces aspects scientifiques, je tiens à remercier Jean pour le rôle important qu'il a joué dans le financement du projet.

Je souhaite également remercier l'ensemble des personnes qui ont travaillé sur le projet dysprosium. Je remercie plus particulièrement Raphael Lopes, avec qui je partage la direction du projet depuis son arrivée dans le groupe en 2018. Son dynamisme, qui contraste avec mon caractère flegmatique, est très motivant pour nos étudiants. Je suis sûr que nous ferons de la belle physique ensemble dans les années à venir. Je remercie tous les étudiants en thèse sur ce projet : Davide Dreon, Chayma Bouazza, Thomas Chalopin, Tanish Satoor, Aurélien Fabre et Jean-Baptiste Bouhiron. Ce sont les forces vives de l'expérience, et la réalisation de chaque projet est conditionnée à leur maîtrise parfaite de tous les rouages de la manip. Je leur souhaite à tous une bonne continuation dans leur carrière, en espérant que leur thèse leur soit aussi profitable que possible. Je remercie également Wilfried Maineult, Leonid Sidorenkov et Vasiliy Makhalov, qui ont effectué un séjour postdoctoral sur ce projet.

Bien que je n'ai pas développé cette part de mon travail dans le manuscript, je suis associé depuis mon arrivée à l'ENS au projet rubidium, et je voudrais remercier toutes les personnes qui y ont contribué. Je remercie Jérôme Beugnon, qui dirige à merveille ce projet. Il a su concevoir une manip qui permet d'aborder une grande variété de problèmes très stimulants. Je remercie de nouveau Jean Dalibard, qui nous éclaire de sa connaissance de la physique à deux dimensions. Je remercie également tous les thésards et postdocs sur ce projet : Rémi Desbuquois, Christof Weitenberg, Laura Corman, Lauriane Chomaz, Tom Bienaimé, Jean-Loup Ville, Monika Aidelsburger, Raphael Saint-Jalm, Patricia Castilho, Edouard Le Cerf, Brice Bakkali-Hassani, Cholé Maury et Yiquan Zou.

Je souhaite enfin remercier les membres du jury, qui m'ont fait l'honneur de participer à l'évaluation de mon travail. Je remercie les rapporteurs de ce mémoire, Tilman Esslinger, Bruno Laburthe-Tolra et Wilhelm Zwerger, ainsi que Jacqueline Bloch et Frédéric Chevy, examinateurs de la soutenance.

Introduction

This manuscript presents a selection of scientific projects performed in the period 2011-2020, as well as perspectives for future research investigations.

My research activities consist in the experimental study of ultracold atomic gases. These laboratory systems, born with the first realizations of Bose-Einstein condensates in 1995, are small ensembles of atoms, well isolated from the environment and manipulated with laser beams and magnetic fields. The variety of confining potential geometries, coherent light-spin couplings and atomic interaction parameters leads to a rich phenomenology of many-body quantum phases.

The interplay between quantum statistics and atomic interactions can be used to generate many-body states in which particles are entangled together. Such collective quantum effects are typically very fragile due to decoherence, via the coupling with the environment. Nevertheless, coherence can be maintained in well isolated systems, and their enhanced susceptibility make them highly sensitive measurement devices. In the absence of entanglement between its constituents, the precision of a sensor is limited by the sum of the quantum fluctuations of its parts – the standard quantum limit. Entanglement between the constituents can be used to correlate their quantum fluctuations, leading to an improvement of sensitivity beyond the standard quantum limit.

We investigated such a quantum-enhanced sensing with ultracold dysprosium atoms, using their electronic spin as a magnetic field probe. Each atomic spin $J = 8$ can be viewed as a set of 16 elementary qubits, that we manipulate using non-linear light shifts to produce non-classical spin states. We demonstrated quantum-enhanced sensing using gaussian squeezed, oversqueezed and N00N states, with a full microscopic characterization that remains challenging in large atomic ensembles. Interpreting the non-linear light shifts as a ferromagnetic interaction between qubits, we could explore a paramagnetic to ferromagnetic quantum phase transition in a mesoscopic system, observing a quantum critical behavior. We discuss extensions of these works to directly probe entanglement between qubit pairs, produce N00N states as protected ground states of a Hamiltonian, and to explore quantum Hall physics once the Bloch sphere is interpreted as a spherical Landau level.

The versatility of ultracold atom settings make them relevant for the quantum simulation of emblematic models of quantum many-body physics. A notorious example is the study of the Fermi Hubbard model with ultracold Fermi gases in optical lattices. This model is expected to capture the main phenomenology of high-T_c superconductors. Recent progress in cold atom experiments allows one to start exploring its phase diagram in a numerically intractable parameter regime.

The projects presented in this manuscript address another important ingredient of quantum simulation with ultracold atoms, namely the simulation of charged particles evolving in a magnetic field. The quantum states of a particle subjected to an orbital

magnetic field are organized in energy bands with a non-trivial topological ordering. The quantum Hall effect occurring in two-dimensional electron gases is a direct manifestation of this topological structure. We discuss here two different implementations of orbital magnetic fields, the first one for atoms confined in optical lattices, the second one for dysprosium atoms using their electronic spin as a synthetic dimension. Future projects will explore the behavior of interacting gases in these structures, aiming to realize Abrikosov vortex lattices in a mean-field regime, as well as analogs of fractional quantum Hall states. We also plan to investigate topological systems of interacting fermions, targeting a topological superfluid phase. This state of matter is expected to host exotic elementary excitations bound at topological defects, the Majorana bound states. The latter are one of the most simple instance of quasi-particles with a non-abelian quantum statistics. A new type of quantum computation could be performed by manipulating these Majorana excitations, the underlying topological properties leading to a strong protection with respect to decoherence.

Most of the projects presented here were performed with an experimental apparatus producing ultracold dysprosium atoms. This project was started in 2014 in the physics institute of Collège de France, after a brief preparation stage at Ecole Normale Supérieure. Besides my supervision as a principal investigator, this project is handled by Jean Dalibard (professor at Collège de France) and Raphael Lopes (since 2018, CNRS researcher). It involved a team of 6 PhD students (3 already defended, 3 ongoing) and 3 postdoctoral researchers. This project aims at using specific properties of atomic dysprosium – large-size electronic spin, rich optical spectrum with isolated narrow transitions – to reach novel regimes for quantum enhanced sensing and simulation of gauge fields. I also present a project on rubidium atoms in optical lattices subjected to a gauge field, that I performed during my postdoctoral stay in Munich, in the group of Prof. Immanuel Bloch.

1 Non-classical states of the electronic spin of dysprosium

We present several projects in which we engineered complex quantum states in the electronic spin of dysprosium atoms. The electronic ground state of dysprosium atoms features an exceptionally large angular momentum $J = 8$, which can be viewed as a mesoscopic quantum magnet. Using spin-dependent light shifts, we could drive this spin in quantum states with highly non-classical behaviors, such as coherent quantum superpositions of distant classical states. We focus the discussion on the sensitivity of these states to rotations (i.e. to magnetic fields inducing Larmor precessions), which is a standard signature of non-classical behavior [1]. Besides this fundamental aspect, the quantum enhancement of sensitivity demonstrated in our studies could also be used for quantum metrology protocols [2]. The projects discussed in this chapter were realized in the period 2017-2019 and presented in three articles [3, 4, 5].

1.1 Quantum-enhanced sensing

1.1.1 Presentation of quantum-enhanced magnetic sensing

When pushing the sensitivity of a measurement apparatus to its limits, the intrinsic quantum fluctuations of its constituents play a prominent role. In most cases, the fluctuations of each element add up independently, leading to a shot noise scaling as $\sqrt{N}$, while the signal increases as the number of elements N. This *standard quantum limit* can be improved by entangling the constituents together, such that their quantum fluctuations are correlated. The control over quantum fluctuations was first developed in quantum optics, via the realization of gaussian squeezed quantum states of light [6, 7, 8, 9]. Such squeezed states can be pictured as coherent states deformed in phase space, so that their quantum fluctuations are reduced along one direction, improving the sensitivity to displacement in phase space when measuring the mean response of the constituents. The sensitivity can be further improved using more complex quantum states, which fluctuations no longer obey gaussian statistics [10]. Ultimately, quantum mechanisms imposes a fundamental bound on sensitivity, rooted in the Heisenberg uncertainty principle, and scaling with the number N of constituents. The projects discussed in this section consist in the generation of such non-gaussian quantum states, and their use for quantum-enhanced sensing.

The system used in our experiments is an uncorrelated ensemble of ^{162}Dy atoms, with an internal electronic spin of angular momentum $J = 8$. This spin can be decomposed – via Majorana's stellar representation [11] – as the collective spin of $2J = 16$ elementary spins 1/2, in a state symmetric upon exchange. Each of these spins can be viewed as an elementary magnetic field sensor, based on its Larmor precession around a magnetic field. The global sensivity of the ensemble of qubits is determined by the quantum state

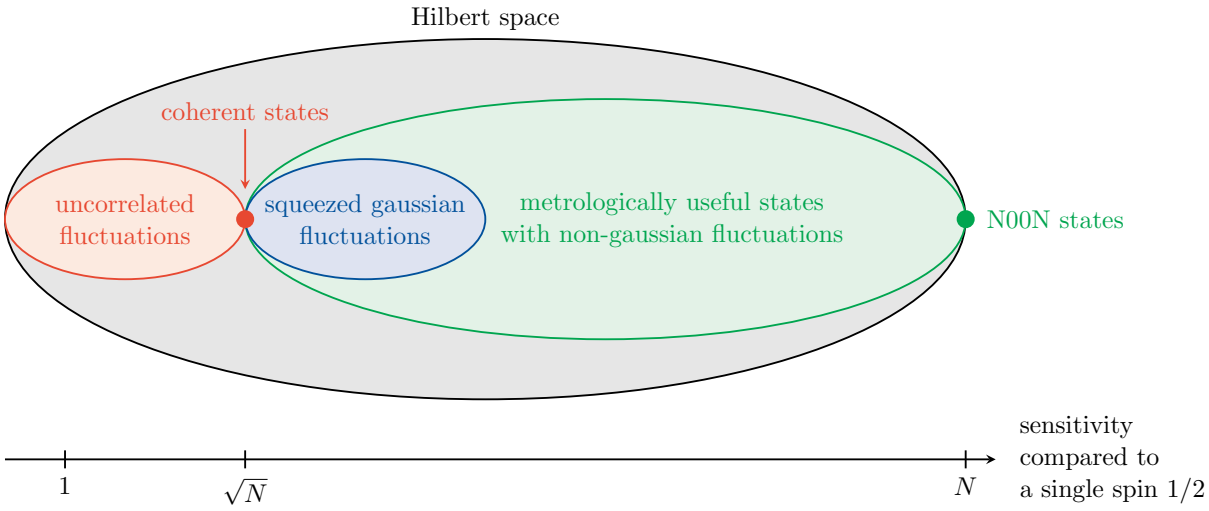

Figure 1.1: Scheme of the different classes of collective spin states discussed in the main text. The x axis refers to the corresponding range of sensitivities compared to the one of an elementary spin 1/2.

of the collective spin and its response to rotation. We present below different classes of collective spin states, and their corresponding magnetic sensitivity (see Fig. 1.1).

Coherent spin states

Measuring the spin projection provides an information on the Larmor precession angle θ, with an uncertainty $\Delta\theta = 1$ for a single measurement with a spin 1/2. A set of N uncorrelated sensors can at best decrease the measurement uncertainty down to $\Delta\theta_{\mathrm{SQL}} = 1/\sqrt{N}$, which requires all spins to be aligned along a common direction $\hat{\mathbf{n}}$. For a collective spin J, such a state corresponds to a *coherent* spin state

$$|\hat{\mathbf{n}}\rangle \equiv |m = J\rangle_{\hat{\mathbf{n}}}\,,$$

maximally polarized along $\hat{\mathbf{n}}$ and with isotropic transverse fluctuations $(\Delta J_{\hat{\mathbf{u}}})^2 = J/2$ (with $\hat{\mathbf{u}} \perp \hat{\mathbf{n}}$) [12].

Squeezing of gaussian quantum fluctuations

The magnetic sensitivity can be improved further using more complex spin states. The most basic family consists of gaussian squeezed states, characterized by reduced quantum fluctuations along a transverse direction $(\Delta J_{\hat{\mathbf{u}}})^2 < J/2$ (with $\hat{\mathbf{u}} \perp \hat{\mathbf{n}}$) [13]. Their quantum fluctuations remain described by gaussian statistics, which imply the saturation of Heisenberg inequality

$$\Delta J_{\hat{\mathbf{u}}}\,\Delta J_{\hat{\mathbf{v}}} \geq \frac{\langle \hat{J}_{\hat{\mathbf{n}}}\rangle}{2}, \quad (\hat{\mathbf{u}} \perp \hat{\mathbf{v}}), (\hat{\mathbf{u}} \perp \hat{\mathbf{n}}), (\hat{\mathbf{n}} \perp \hat{\mathbf{v}}).$$

These states outperform coherent spin states when probing magnetic fields aligned along $\hat{\mathbf{v}}$. More precisely, the Larmor rotation induced by the magnetic field can be deduced from a projection measurement of the collective spin, with an uncertainty [14]

$$\Delta\theta = \Delta\theta_{\mathrm{SQL}}/\sqrt{\bar{G}}, \quad \bar{G} = \frac{2\langle \hat{J}_{\hat{\mathbf{n}}}\rangle^2}{J(\Delta J_{\hat{\mathbf{u}}})^2},$$

where $\bar{G}$ is the *metrological gain* with respect to the standard quantum limit.

Non-gaussian spin states

When pushing the quadrature squeezing along $\hat{\mathbf{u}}$ down to $\Delta J_{\hat{\mathbf{u}}} \sim 1$, the spin fluctuations along $\hat{\mathbf{v}}$ become of order $\Delta J_{\hat{\mathbf{v}}} \sim J$, i.e. comparable to the extent of the generalized Bloch sphere. In this *oversqueezed* regime, the spin projection fluctuations are no longer described by gaussian statistics and the metrological gain $\bar{G}$ is reduced.

More generally, non-gaussian spin states can also be used for quantum metrology, albeit involving more complex measurement protocols. For a given pure quantum state, the optimal sensitivity is reached for magnetic fields oriented along the direction $\hat{\mathbf{v}}$ along which the spin projection uncertainty is maximum. The corresponding maximum metrological gain is the so-called Cramér-Rao bound, and reads [15]

$$G = \frac{2(\Delta J_{\hat{\mathbf{v}}})^2}{J}.$$

We stress that reaching this bound may involve measuring very complex observables, involving high-order spin moments. We finally mention the Heisenberg limit of sensitivity $G = 2J$, which is the ultimate sensitivity allowed for a spin J. It is reached for the states maximizing the spin projection uncertainty along a given direction $\hat{\mathbf{v}}$, i.e. N00N states of the kind $|J\rangle_{\hat{\mathbf{v}}} + |-J\rangle_{\hat{\mathbf{v}}}$. This maximum gain exceeds the range of metrological gains $\bar{G}$ that can be achieved using gaussian spin states, as pictured in Fig. 1.1.

1.1.2 Context of our projects

Quantum-enhanced sensing has been realized in a large variety of physical systems. We focus here on experiments performed with Bose-Einstein condensates [1], in close comparison with the ones performed in our group. There, an internal degree of freedom plays the role of the elementary spin 1/2, and the meter consists in the collection of N atoms in the same spatial mode, with typically $N \sim 100 - 10^5$. Quantum-enhanced sensing can be reached by entangling the atoms together via interactions. More precisely, the collective spin is driven by a non-linear Hamiltonian

$$\hat{H} = \hbar\chi \hat{J}_x^2, \quad \hbar\chi = U_{\uparrow\uparrow} + U_{\downarrow\downarrow} - 2U_{\uparrow\downarrow},$$

where $U_{\sigma\sigma'}$ is the interaction amplitude for a pair of atoms in the spin states σ and σ'. The non-linear dynamics under this *one-axis twisting* Hamiltonian is shown in Fig. 1.2 [13]. This mechanism was used in numerous experiments to produce gaussian squeezed states [16, 17, 18, 19, 20]. More recently, non-gaussian *oversqueezed* states were investigated in [21], the authors demonstrating a quantum enhancement of sensitivity provided one measures higher-order spin moments. Nevertheless, the sensitivities reached in these experiments remain far from the Heisenberg limit, due to decoherence in the state preparation and to the difficulty to access the required highest-order spin correlators.

In our experiment, we transposed these concepts to a gas of ^{162}Dy atoms, where the electronic spin of each atom plays the role of the collective spin introduced above. The electronic spin length $J = 8$ then corresponds to the collective spin of 16 'hidden' qubits. In our setup, the non-linear spin dynamics no longer occurs via inter-atomic interactions, the atoms evolving independently from each other. Rather, each electronic spin is driven by an off-resonant light beam producing a quadratic Zeeman light shift. The asset of our system is the restricted size of the Hilbert space dimension $2J + 1 = 17$, much smaller than the size $2^{2J} = 65\,536$ for an ensemble of $2J$ qubits (including the non-exchange-symmetric subspace). This restricted size limits the number of decoherence

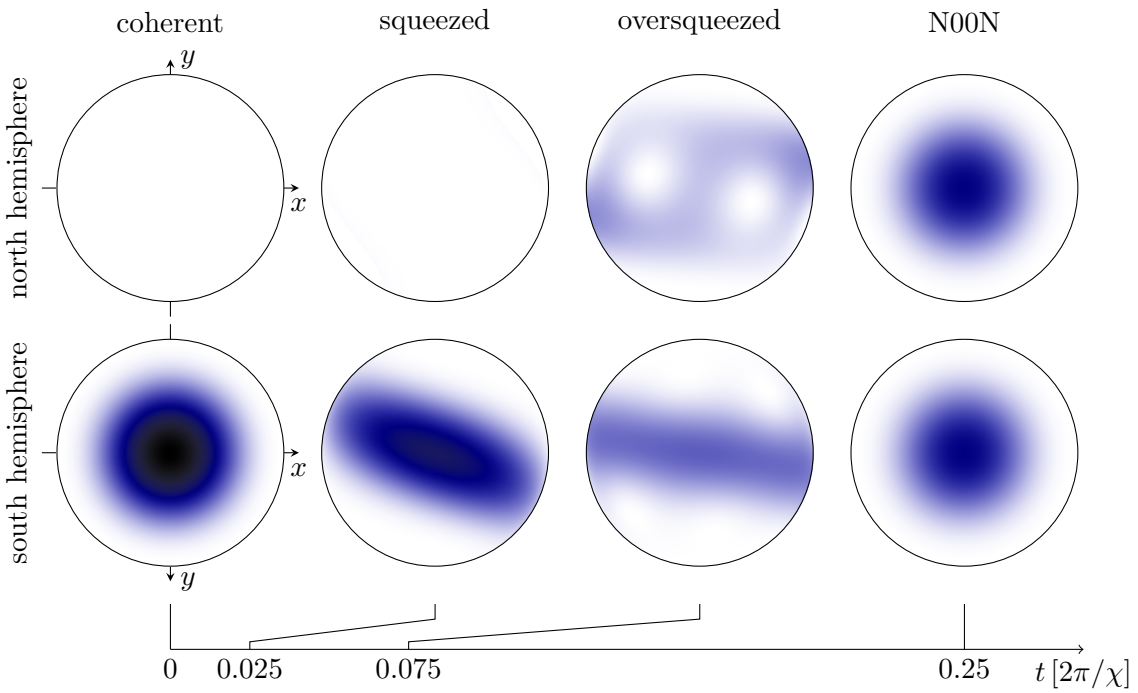

Figure 1.2: One-axis twisting dynamics of a spin $J = 8$, starting in a coherent state $|m = -J\rangle_z$. We plot the Husimi Q function on the generalized Bloch sphere, with separate views of the north and south hemispheres. After a short evolution time the spin fluctuations are squeezed (still with a gaussian distribution). For longer times the spin spreads around the entire xz meridian, leading to oversqueezed states. Such states feature a short-scale structure, with holes in the distribution interpreted hereafter as vortices. For $t = \pi/(2\chi)$, the system reaches a N00N state, superposition of coherent states pointing north and south.

channels without decreasing the metrological capabilities from quantum compression. In our system, we could thus explore non-linear spin dynamics at long times, passing through squeezed, oversqueezed and N00N states (see Fig. 1.2). For the non-gaussian oversqueezed and N00N states, we revealed the complexity of the measurements required to reach the Cramér-Rao bound on sensitivity.

1.1.3 Non-linear spin dynamics

In our experiments, we drive non-linear spin dynamics via the spin-dependent light shifts of an off-resonant laser beam. We use laser light close to a narrow optical transition of resonant wavelength $\lambda = 626.1\,\mathrm{nm}$, with a linear polarization along x, thus producing a light shift

$$\hat{H} = \hbar\chi \hat{J}_x^2, \quad \hbar\chi = -\frac{1}{(J+1)(2J+1)} \frac{3\pi c^2 \Gamma}{2\omega_0^3 \Delta} I.$$

The states produced after the one-axis twisting dynamics are probed using spin projection measurements. We use a magnetic field gradient to separate the different spin components along $\hat{\mathbf{n}}$, giving access to the spin projection probabilities $\Pi_m(\hat{\mathbf{n}})$.

We show in Fig. 1.3 examples of spin projection measurements for squeezed, oversqueezed and N00N states. For short evolution times we measure a squeezing of spin

fluctuations, which remain well described by gaussian statistics. For longer times, in the oversqueezing regime, the spin fluctuations exhibit a complex structure. For the specific time $\chi t = \pi/2$, the measurements are consistent with a N00N state $|+J\rangle_z + |-J\rangle_z$: projections along $m = \pm J$ along z, and characteristic oscillation of the parity of the spin projection in the xy plane.

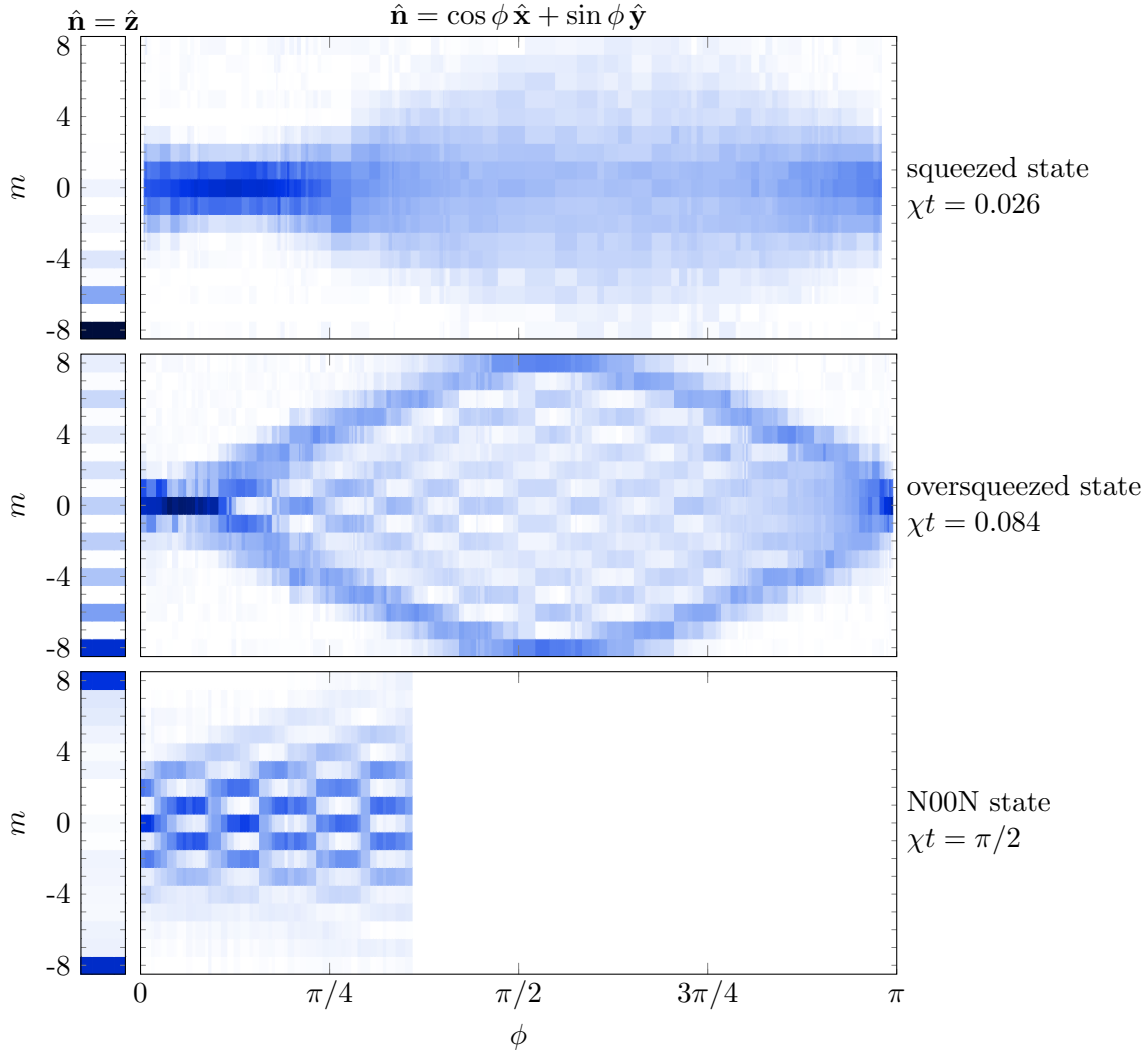

Figure 1.3: Spin projection measurements performed for squeezed, oversqueezed and N00N states. The projection is performed along $\hat{\mathbf{z}}$ (left panels) and in the xy plane (right panels), parametrized by the azimuthal angle ϕ.

Optimal quantum sensing

The squeezed states produced after a short evolution can be used to perform magnetic sensing beyond the standard quantum limit. The reduction of a spin projection quadrature implies that the *mean spin* projection gives a more precise information on the Larmor rotation angle, compared to a coherent spin state. For such gaussian states, the measurement of first-order spin moments is sufficient to reach the Crámer-Rao bound, i.e. the optimal sensitivity granted by the considered state.

For oversqueezed and N00N states, the measured spin projection probabilities exhibit highly contrasted short-scale variations, which can be used as a much more sensitive

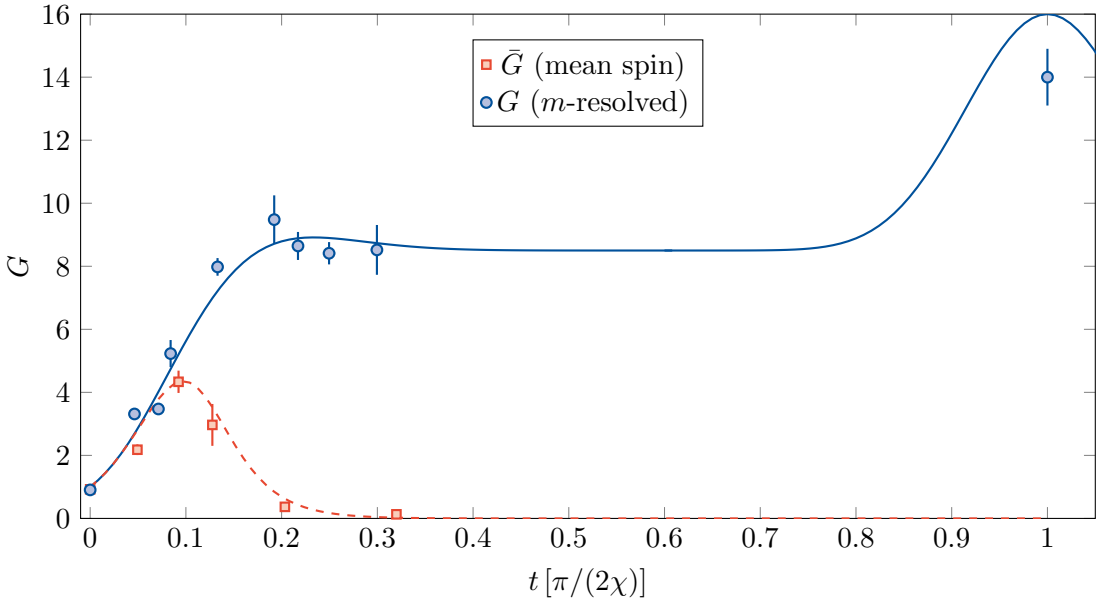

Figure 1.4: Metrological gain in magnetic sensitivity as a function of the non-linear evolution time, for two observables, namely the mean spin projection (red squares) and the m-resolved spin projection (blue circles). The regimes of gaussian squeezed, oversqueezed and N00N states correspond to the regions $\frac{2}{\pi}\chi t < 0.1$, $0.1 < \frac{2}{\pi}\chi t < 0.3$ and $\frac{2}{\pi}\chi t = 1$, respectively.

probe of Larmor rotations. Importantly, these variations would be washed out if our measurements were limited to low-order spin moments. For these non-gaussian states, single-m resolution is thus mandatory to reach optimal sensitivity.

We show in Fig. 1.4 the metrological gains measured from the mean spin projection (red dots) or using the m-resolved spin projections. We confirm that the two observables lead to similar magnetic sensitivities for gaussian squeezed states. We reach the Cramér-Rao bound $G \simeq J$ for oversqueezed states when using m-resolved measurements, and approach the Heisenberg limit for N00N states. We stress that the optimal character of m-resolved measurements is a remarkable property, based on the special structure of quantum states reached via one-axis twisting dynamics [22].

Retrieving the hidden spin composition

The gain in sensitivity measured in our experiments stems from the specific quantum fluctuations of the spin J – reduction of a spin quadrature for gaussian squeezed states, small-scale structuring for oversqueezed and N00N states. When considering the spin J as a collective spin associated to $2J$ spins $1/2$, the metrological gain can be linked to the depth of quantum entanglement between the elementary spins [23, 24].

The physical existence of $2J = 16$ elementary spins $1/2$ in the electronic spin $J = 8$ of dysprosium atoms is not obvious. Indeed, we remind that this degree of freedom results from four electron vacancies in the $^4f^{10}$ electronic shell of atomic dysprosium, leading to an orbital angular momentum $L = 6$ and a spin $S = 2$. Nevertheless, we have been able to retrieve the hidden elementary spin composition from the measurement of the Husimi Q function. We remind that the Husimi function is defined as the squared overlap with a

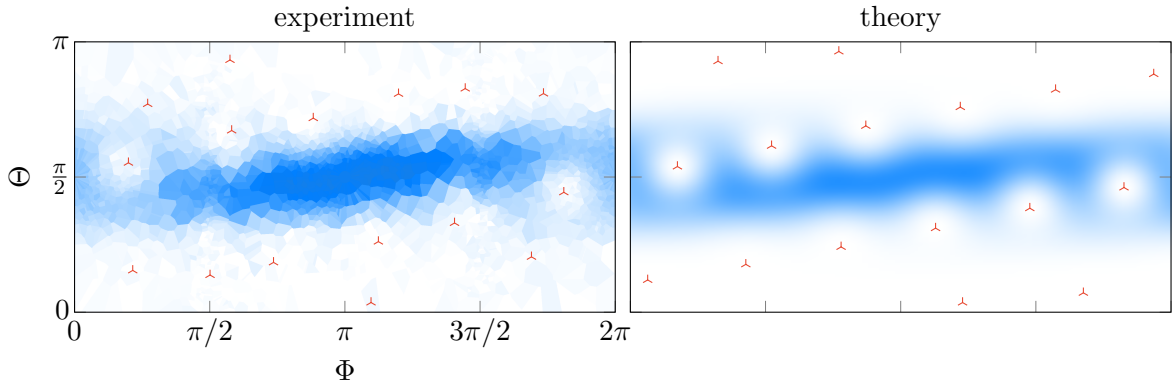

Figure 1.5: Husimi functions measured and computed for a quantum state produced after a non-linear evolution of duration $\chi t = 0.55$. A fit with the ansatz (1.1) allows us to retrieve the positions of the 16 zeros of the Husimi function (opposite to the Majorana stars).

coherent state pointing along $\hat{\mathbf{n}}$, i.e., for a pure state $|\psi\rangle$,

$$Q(\hat{\mathbf{n}}) \equiv |\,\langle\psi|J\rangle_{\hat{\mathbf{n}}}\,|^2.$$

It can also be expressed as the product of the $2J$ Husimi functions of the elementary qubits, as

$$Q(\hat{\mathbf{n}}) \propto \prod_{i=1}^{2J}(1+\hat{\mathbf{n}}\cdot\hat{\mathbf{u}}_i), \tag{1.1}$$

where the $\hat{\mathbf{u}}_i$ are the Bloch vector orientations of the qubits ('Majorana stars'). From (1.1), one notices that the Husimi function cancels for all directions $\hat{\mathbf{n}}$ opposite to one of the Majorana stars.

We used this property to retrieve the 16 orientations of the qubits hidden in the electronic spin $J = 8$ of dysprosium atoms. We measured the Husimi function of a given quantum state via the spin projection probability in the stretched state $|J\rangle_{\hat{\mathbf{n}}}$, for projection axes $\hat{\mathbf{n}}$ spanning the entire Bloch sphere. For oversqueezed states, the spin distribution is extended enough for several zeros of the Husimi function to be directly visible. Moreover, the whole set of Majorana stars can be reliably fitted from the global shape of the measured Husimi function. To our knowledge, this measurement constitutes the first observation of the Majorana stars of a collective spin.

1.2 Ground state of a non-linear spin model

The generation of non-classical spin states discussed so far was based on the quenching of a non-linear spin coupling. We showed that the resulting one-axis twisting dynamics can potentially give access to N00N states. Such a route to maximally sensitive quantum states remains a remarkable exception. Indeed, for more complex systems with additional degrees of freedom or submitted to decoherence, one generally cannot design simple dynamical protocols to generate highly non-classical states.

In this section we discuss a different scheme, based on the adiabatic driving of a quantum system through a quantum phase transition [25]. Compared to the states generated via dynamic evolution, an adiabatic process produces non-classical states as steady

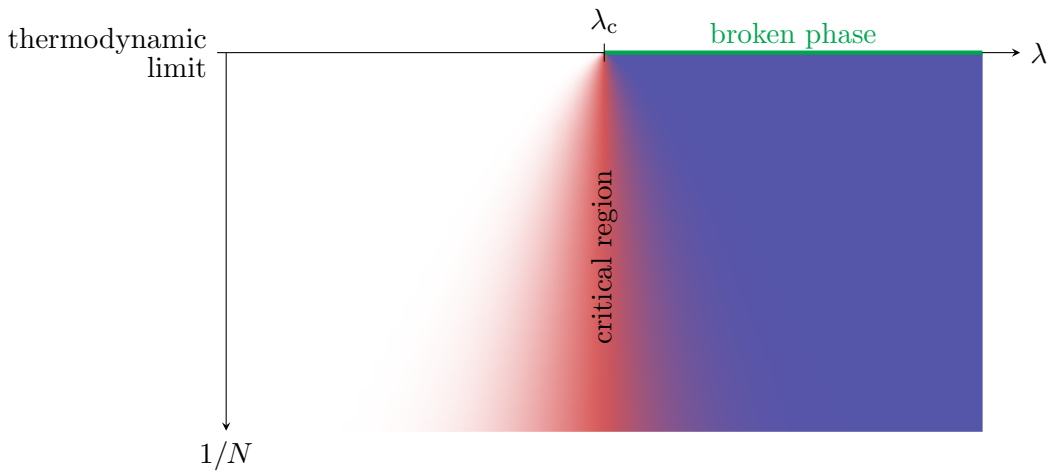

Figure 1.6: Generic phase diagram close to a quantum phase transition. In the thermodynamic limit, the system exhibits two different phases separated by the critical point λ_c, with one phase spontaneously breaking an underlying symmetry. In a finite system, the transition is smoothened into a quantum critical region, shown here in red.

states with a well-defined protection from environmental noise or finite temperature – determined by the energy gap to higher energy states.

Adiabatic driving through a quantum phase transition

As shown in Fig. 1.6, we consider a quantum system whose dynamics depends on a parameter λ, such that the critical point $\lambda = \lambda_c$ separates two different many-body phases in the thermodynamic limit. We assume that the phase for $\lambda < \lambda_c$ exhibits a single many-body ground state, protected by an energy gap. For $\lambda > \lambda_c$, the ground state corresponds to a different phase, characterized for example by a broken $\mathbb{Z}_2$ symmetry, as relevant for the experiments discussed in this section.

In the thermodynamic limit, the energy gap protecting the ground state vanishes at the phase transition point, such that adiabatic driving though the critical point cannot be achieved. For a second-order phase transition, crossing the critical point at finite speed inevitably produces defects via the Kibble-Zurek mechanism, with a defect density decreasing for slower ramps [26, 27]. We consider here a finite-size system, for which the system always remains gapped. As shown in Fig. 1.7, two energy gaps have to be considered in the presence of a $\mathbb{Z}_2$ symmetry: (i) the gap Δ separating the ground state to excited states of same symmetry, (ii) the gap δ separating the ground state to excited states of opposite symmetry. Both gaps are strongly reduced at the vicinity of the phase transition, in the critical region. In the broken phase, the gap Δ increases again, such that the system is protected from perturbations preserving the symmetry. On the contrary, the gap δ is highly reduced, manifesting the existence of almost degenerate ground states with broken symmetry.

Ground state of the Lipkin model

We have studied this phenomenology by preparing the ground state of a non-linear spin model, described by the Hamiltonian

$$\hat{H}(\lambda) = -\frac{\lambda}{2J-1}\hat{J}_x^2 + \hat{J}_z. \tag{1.2}$$

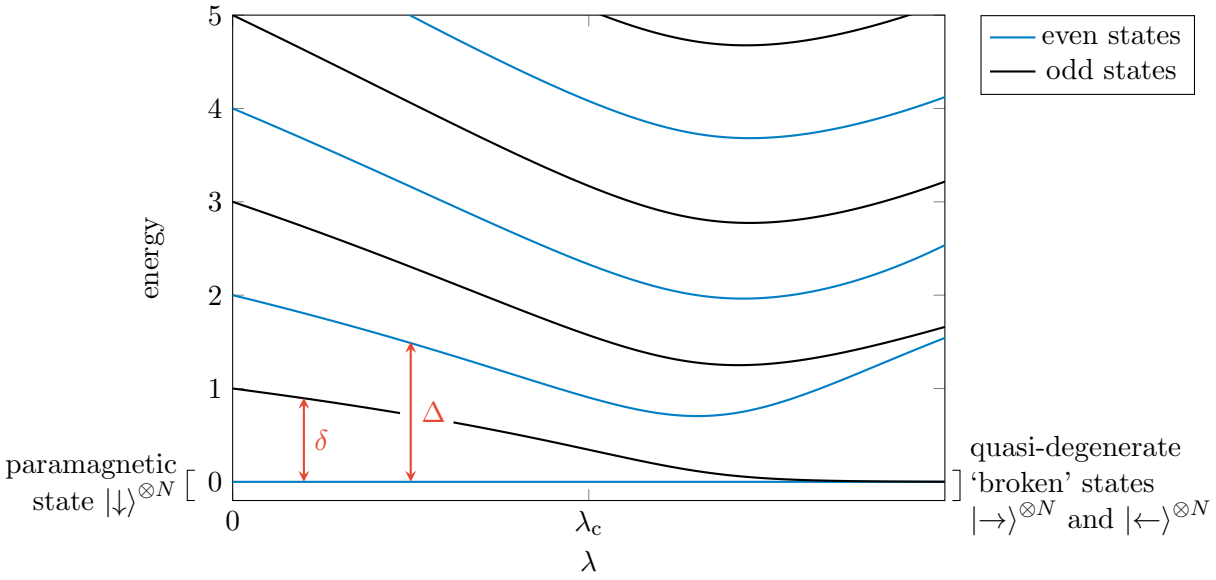

Figure 1.7: Energy spectrum of the Lipkin model as a function of the ferromagnetic coupling strength λ (ground-state energy set to zero). In the thermodynamic limit, the critical point $\lambda_c = 1$ separates a paramagnetic phase ($\lambda < \lambda_c$) and a ferromagnetic phase ($\lambda > \lambda_c$). In our finite-size system the ferromagnetic phase exhibits two quasi-degenerate ground states, corresponding to two broken symmetry states. The low-energy dynamics is governed by two gaps, the gap Δ to the even-parity excited states relevant for symmetry-conserving perturbations, and the gap δ to the odd-parity sector relevant for symmetry-breaking perturbations.

This model was introduced in a context of nuclear physics by Lipkin, Meshkov and Glick [28]. It is symmetric under reflection of the spin along x, corresponding to a conservation of the parity

$$\hat{P}_z \equiv \sum_{m=-J}^{J} (-1)^m \left|m\right\rangle_z \left\langle m\right|_z$$

of the spin projection along z. In the thermodynamic limit $J \to \infty$, the ground state of the Lipkin model exhibits a quantum phase transition at the critical point $\lambda_c = 1$. For $\lambda < \lambda_c$, the ground state $\left|m = -J\right\rangle_z$ is parallel to the z Zeeman field, consistent with a paramagnet. For $\lambda > \lambda_c$, the system exhibits two degenerate ground states oriented in the xz plane, corresponding to ferromagnetic states. Each of these quasi-classical ground states has a non-zero magnetization along x, thus breaking the underlying reflection symmetry.

We studied experimentally the characteristics of this ground state, by engineering the Hamiltonian (1.2) using a combination of a second-order light shift ($\hat{J}_x^2$ term) and a magnetic field ($\hat{J}_z$ term). The ground state of $\hat{H}(\lambda)$ is produced by slowly ramping up the non-linear spin coupling. We characterized the ground state by measuring the projection probabilities $\Pi_m(\hat{\mathbf{n}})$ along the directions $\hat{\mathbf{n}} = \hat{\mathbf{x}}, \hat{\mathbf{y}}, \hat{\mathbf{z}}$ (see Fig. 1.8). The measurements along $\hat{\mathbf{x}}$ show a bifurcation between a single-peak distribution centered around zero for $\lambda < 1$ and a double-peak distribution for $\lambda > 1$, corresponding to the two broken states. Importantly, both peaks are present with almost equal weights for each realization of the experiment. The system is thus not projected, as a whole, on a single broken state. This behavior is corroborated by the projection measurements along $\hat{\mathbf{z}}$, which shows significant

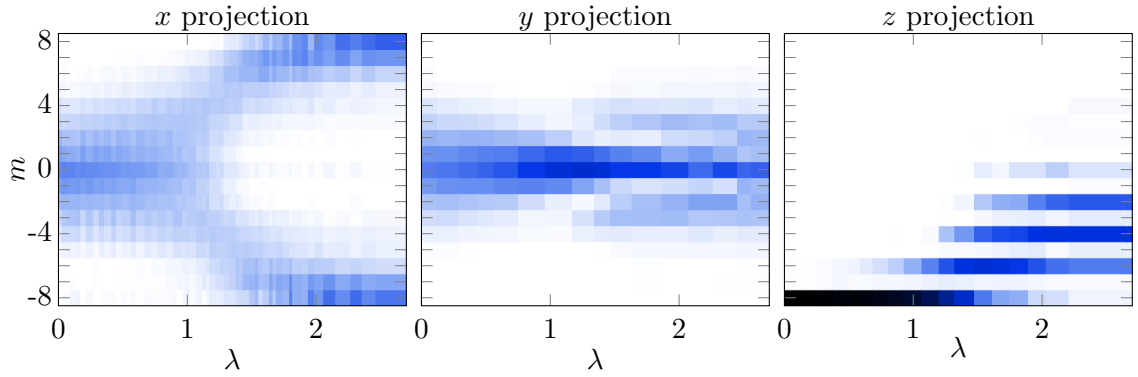

Figure 1.8: Measured spin projection probabilities in the ground state of the LMG model, as a function of the ferromagnetic coupling amplitude λ. The x projections exhibit a bifurcation revealing a crossover to a ferromagnetic behavior for $\lambda > 1$. The y projections reveal a squeezed spin state around the critical point $\lambda_c = 1$. The z projections are consistent with conservation of the parity even in the 'ferromagnetic' phase: the $\mathbb{Z}_2$ symmetry is not spontaneously broken in our finite-size system.

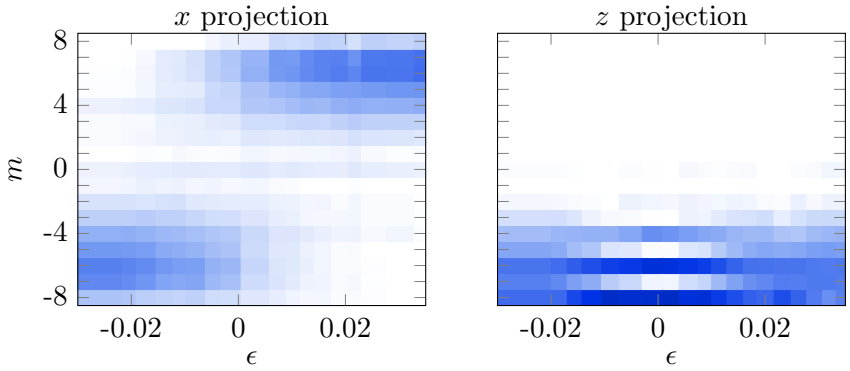

Figure 1.9: Measured spin projection probabilities in the ground state of the LMG model for $\lambda = 1.40(3)$, as a function of the amplitude ϵ of an additional Zeeman field along x.

probabilities on even $|m\rangle$ states only, i.e. parity is conserved even in the 'ferromagnetic' region $\lambda > 1$. In this regime, the spin state thus corresponds to a coherent superposition of the two quasi-classical broken states.

To recover a truly ferromagnetic state for $\lambda > \lambda_c$, we introduced a controlled symmetry-breaking perturbation, via an additional Zeeman field ϵJ_x. We show in Fig. 1.9 the projection probabilities along x and z, measured in the ferromagnetic region for $\lambda = 1.40(3)$. We find that a small perturbation $\epsilon \sim 0.02$ is sufficient to transfer the state on one of the broken states, characterized by a non-zero magnetization $\langle \hat{J}_x \rangle$ along x with a concomitant drop of the mean parity $\langle P_z \rangle$ to zero. This experiment illustrates a fundamental mechanism of second-order phase transitions, namely the link between the onset of an order parameter and the breaking of an underlying symmetry.

Low-energy excitations

We investigated the low-energy excitations of the system by measuring the time response of the system following a small perturbation. We used either symmetry-breaking or symmetry-conserving perturbations to access in separate experiments the two relevant

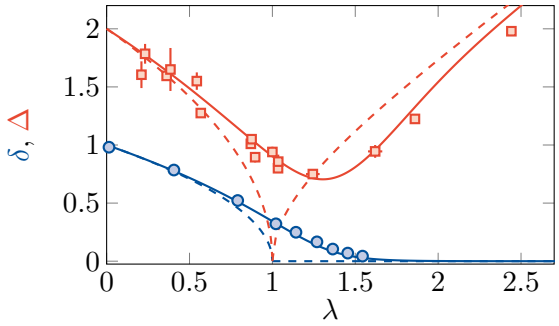

Figure 1.10: Measured gaps Δ and δ to the even- and odd-parity sectors as a function of the ferromagnetic coupling strength.

gaps introduced above.

The gap Δ to the even-parity sector exhibits a minimum around the critical point, reminiscent of the gap closing at $\lambda = \lambda_c$ in the thermodynamic limit. In a finite-size system, the gap no longer cancels but features a minimum scaling as $J^{-1/3}$.

The gap δ to the odd-parity sector takes very small values in the ferromagnetic region $\lambda > \lambda_c$, consistent with the approximate degeneracy of the pair of ferromagnetic states. In our experiment we can resolve this gap down to $\delta_{\min} = 0.05$, below which residual magnetic field fluctuations lift the degeneracy between the two broken states. In the regime $\delta_{\min} < \delta \ll 1$, we were able to prepare the system in a given broken state, and observe the subsequent oscillation between the two broken states at the frequency δ. Such a coherent evolution can be interpreted as a macroscopic tunneling between distinct quasi-classical states.

Potential quantum-enhanced sensitivity

The produced ground states feature characteristic properties of quantum-enhanced sensitivity to magnetic fields. First, the measured probabilities along $\hat{\mathbf{y}}$ are squeezed around $|m = 0\rangle_y$, down to a minimum projection variance $(\Delta J_y)^2 = 1.4(1)$ for $\lambda \simeq 1$, well below the standard quantum limit $(\Delta J_y)^2 = J/2 = 4$ (see Fig. 1.8). This value is compatible with a metrological gain of magnetic sensitivity up to $\bar{G} = 2.6(2)$ above the standard quantum limit, by measuring the rotation of the mean spin (see Fig. 1.11). This behavior illustrates a generic feature of critical systems, associated with an enhancement of fluctuations and susceptibilities, thus amplifying the sensitivity to external parameters [29].

In our finite-size system, the ground state prepared for $\lambda > \lambda_c$ does not break the $\mathbb{Z}_2$ symmetry, being a coherent superposition of the two broken states expected in the ferromagnetic phase. Away from the critical point, these two states are distant in phase space, such that one can dub them 'Schrödinger' kitten states, in reference to cat states, i.e. superpositions of macroscopically different quantum states. Such states could be used to enhance the metrological gain and approach the Heisenberg limit (see Fig. 1.11).

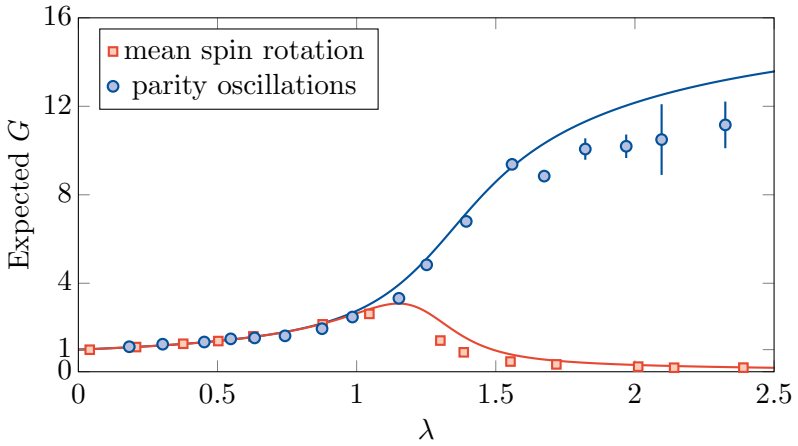

Figure 1.11: Metrological gain expected by measuring the mean spin precession or the oscillation of the parity of the spin projection, using the ground state of the Lipkin model. The points corresponds to the expected gains given the measured characteristics of the states produced in the experiments.

1.3 Non-classical spin states: outlook

1.3.1 Measuring hidden entanglement

The electronic spin $J = 8$ of dysprosium atoms can be viewed as a set of 16 elementary spins 1/2. An important feature of the non-classical states produced in our experiments is the hidden entanglement between the underlying qubits. We discuss here a future project aiming at probing pairwise entanglement within the electronic spin of dysprosium.

As shown in [30], entanglement between pairs of qubits is intimately linked to quadrature squeezing of the collective spin associated with the qubit ensemble. This connection between entanglement and collective spin fluctuations has been used to reveal pairwise entanglement in atomic ensembles [1]. Nevertheless, a direct proof of entanglement requires extracting a pair of qubits and probing their quantum correlations e.g. via Bell-type protocols, which remains extremely challenging.

In our system, extracting a pair of qubits is impossible at low energy, the electronic spin $J = 8$ being 'unbreakable'. Intuitively, qubits can be extracted or added by coupling the spin J to another electronic level with $J' \neq J$. We discuss here the particular case in which one resonantly couples the spin J to a level $J' = J - 1$ using a resonant optical transition. Remarkably, the absorption cross-section gives a direct access to the two-qubit reduced density matrix, in a state defined by the laser polarization.

We consider a pure state $|\psi\rangle$ of a spin J, which can be viewed as a set of $2J$ qubits in an exchange symmetric state. The two-qubit density matrix can itself be expressed as a density matrix of a spin 1. It can be obtained by tracing out the $2J - 2$ remaining qubits, which form a collective spin $J' = J - 1$. In this collective spin representation, the two-qubit density matrix can be expressed as

$$\langle q'| \hat{\rho}_{\text{pair}} |q\rangle = \sum_{m=-(J-1)}^{J-1} \langle J-1, m; 1, q'|\psi\rangle \langle \psi|J-1, m; 1, q\rangle \,, \tag{1.3}$$

with $q, q' \in \{-1, 0, 1\}$.

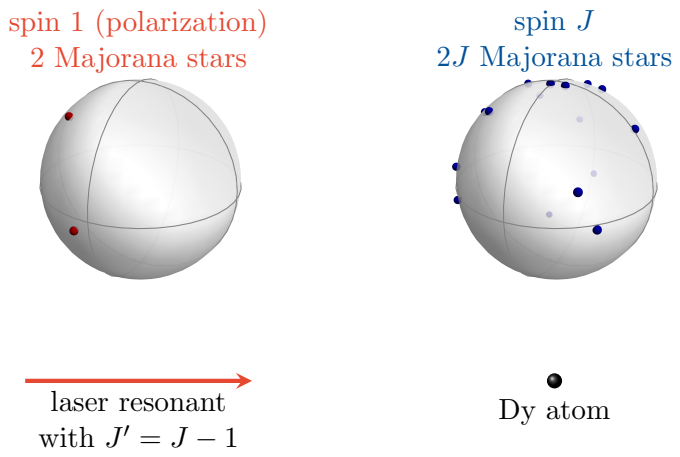

Figure 1.12: Scheme of the measurement of the two-qubit density matrix. The electronic spin J of dysprosium atoms can be viewed as a collection of $2J$ elementary qubits. To probe the two-qubit density matrix, we measure the absorption of a laser beam resonant with a transition to $J' = J - 1$. The photon can itself be viewed as a quantum object of spin $L = 1$, equivalent to a pair of qubits defined by the photon polarization. The absorption rate towards an electronic state of angular momentum $J' = J - 1$ gives access to the probability to find pairs of qubits in a state defined by the laser polarization.

The connection between the pair density matrix and the absorption cross-section is rooted in the equivalence between the states $|1, q\rangle$ of a spin 1 and the polarization states $\boldsymbol{\epsilon}_q$:

$$\begin{aligned} |1, q = \pm 1\rangle &\quad \leftrightarrow \quad \boldsymbol{\epsilon}_{\pm 1} = (\hat{\mathbf{x}} \pm \mathrm{i}\hat{\mathbf{y}})/\sqrt{2}, \\ |1, q = 0\rangle &\quad \leftrightarrow \quad \boldsymbol{\epsilon}_0 = \hat{\mathbf{z}}. \end{aligned}$$

Let us now consider the interaction with a laser field of electric field amplitude $\mathbf{E} = E\boldsymbol{\epsilon}$, resonant with an excited electronic state of angular momentum $J' = J-1$. The probability of absorption reads, in the short-time limit,

$$P_{abs} = \langle\psi| \left(\mathbf{d} \cdot \mathbf{E}\right)^\dagger \Pi_{J'=J-1} \mathbf{d} \cdot \mathbf{E} \, |\psi\rangle \, t^2,$$

where $\Pi_{J'} = \sum_{|\psi'\rangle} |\psi'\rangle \langle\psi'|$ projects on the resonant excited electronic state. Using Wigner-Eckart theorem, we write the dipole q-component as

$$d_q = \sum_{J'=J-1}^{J+1} \langle J'||\mathbf{d}||J\rangle \sum_{m,m'} |J', m'\rangle \langle J, m; 1, q|J', m'\rangle \langle J, m| \,.$$

Decomposing the polarization as

$$\boldsymbol{\epsilon} = \sum_{q=-1}^{1} \epsilon_q \mathbf{e}_q,$$

we obtain the expression for the absorption probability

$$P_{\mathrm{abs}} = (\Omega t)^2 \sum_{q,q'} \epsilon^*_{q'} \epsilon_q a_{q,q'},$$

where $\Omega = \langle J-1||\mathbf{d}||J\rangle E$ and

$$a_{q,q'} = \sum_{m_1,m_2,m'} \langle\psi|J,m_1\rangle \langle J,m_2|\psi\rangle \langle J,m_1;1,q|J-1,m'\rangle \langle J-1,m'|J,m_2;1,q'\rangle .$$

After simple algebraic manipulations, we write

$$\begin{aligned} a_{q,q'} &= \frac{2J-1}{2J+1}(-1)^{q+q'} \sum_{m'} \langle\psi|J-1,m';1,-q\rangle \langle J-1,m';1,-q'|\psi\rangle , \\ &= \frac{2J-1}{2J+1}(-1)^{q+q'} \langle -q'| \hat{\rho}_{\text{pair}} |-q\rangle . \end{aligned}$$

We then obtain the final expression

$$P_{abs} = \frac{2J-1}{2J+1}(\Omega t)^2 \langle \boldsymbol{\epsilon}^*| \hat{\rho}_{\text{pair}} |\boldsymbol{\epsilon}^*\rangle ,$$

where the ket $|\boldsymbol{\epsilon}^*\rangle$ corresponds to the spin-1 state aligned with the time-reversed polarization $\boldsymbol{\epsilon}^*$, such that $(\boldsymbol{\epsilon}^*)_q = (\boldsymbol{\epsilon}_{-q})^*$. Equivalently, this result can be expressed in terms of an absorption cross-section

$$\sigma(\boldsymbol{\epsilon}) = \frac{3\lambda^2}{2\pi}\langle\boldsymbol{\epsilon}^*|\hat{\rho}_{\text{pair}}|\boldsymbol{\epsilon}^*\rangle, \tag{1.4}$$

where λ is the light wavelength. Physically, the formula (1.4) shows that the light absorption can be viewed as a process of extraction of a pair of qubits in the state $|\boldsymbol{\epsilon}^*\rangle$.

The qubit pair properties can then be retrieved via the tomographic reconstruction of the reduced pair density, based on the measurement of the light absorption cross section for various polarizations. In particular, the amount of pairwise entanglement, generally expressed in terms of the so-called *concurrence*, is directly related to the pair density matrix [31].

1.3.2 Protected N00N states

The experiments discussed in this chapter are based on spin-dependent light shifts, which give rise to first- and second-order spin couplings. An interesting research direction could be the extension to higher order couplings. In particular, a coupling proportional to the parity P_z – a spin operator of maximal order – can stabilize the N00N state $|J\rangle_x + |-J\rangle_x$ as the ground state of the Hamiltonian

$$\hat{H} = -\hat{J}_x^2 + \hat{P}_z.$$

Such a highly entangled ground state is closely connected to complex states of matter, such as fragmented Bose condensates [32] and quantum time crystals (in the absence of external driving) [33]. These exotic states are expected to occur in long-range interacting systems, as simulated in our system by a spin coupling of high rank.

The generation of high-order spin couplings would be based on the spatial separation of the different spin levels, combined with an additional potential to produce differential energy shifts. We illustrate this idea in Fig. 1.13, which presents a protocol to generate a potential proportional to the parity by combining a magnetic field gradient and an optical lattice.

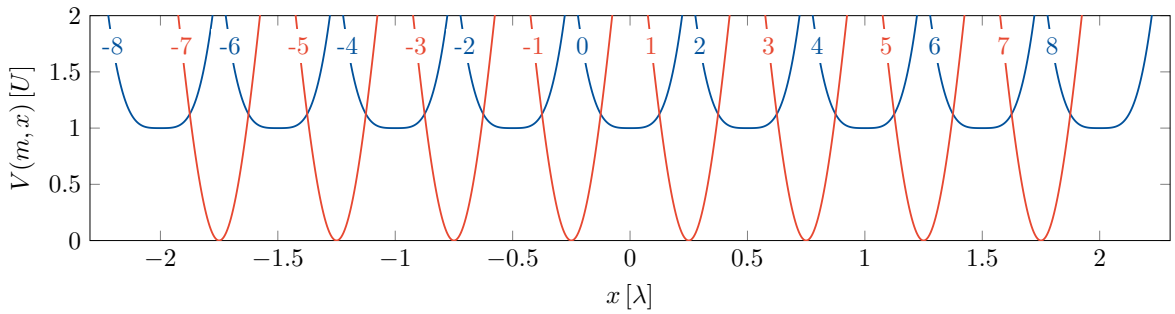

Figure 1.13: Potential subjected to each magnetic projection state $-J \leq m \leq J$ by combining a harmonic trap, a magnetic field gradient and an optical lattice. The magnetic gradient leads to a spatial shift of the harmonic potential proportional to m[†]. When the shift between successive m states equals half the lattice spacing, the potential minima are modulated in energy as the parity $(-1)^m$. Typically, this potential would be produced using a confining potential of frequency $\omega = 2\pi \times 100\,\mathrm{kHz}$, a magnetic gradient $G = 100\,\mathrm{G/cm}$, and a lattice depth $U = h \times 1\,\mathrm{kHz}$, with a lattice wavelength $\lambda = 1\,\mu\mathrm{m}$.

1.3.3 Quantum Hall physics on the Bloch sphere

The observation of small-scale holes in the Husimi distribution can be related to the existence of quantized vortices in the Husimi wavefunction. For a quantum state $|\psi\rangle$ of a spin J, the Husimi wavefunction is defined over the Bloch sphere as

$$\psi(\hat{\mathbf{n}}) = \langle J|_{\hat{\mathbf{n}}}\,|\psi\rangle\,.$$

Each Majorana star then corresponds to a quantum vortex of charge 1 [11, 34]. This interpretation maps the spin J on a lowest Landau level defined on the sphere with $2J$ flux quanta [35].

This structure can a priori give access to quantum Hall phenomena. We assume the dynamics to be restricted to the spin degree of freedom, and consider the arrangement of the $2J$ vortices determined by the spin-dependent interactions between atoms.

We first consider a mean-field regime, in which the number N of condensed atoms largely exceed the vortex number $2J$. We expect condensation into a single spin state, characterized by a vortex arrangement that depends on the spin-dependent interactions between atoms [36]. The latter are described by $J+1 = 9$ independent coupling constants g_K, where K is the total angular momentum of a colliding atom pair ($0 \leq K \leq 2J$, K even). To keep the discussion simple, we focus on the case where g_{2J} is positive and much larger than the other coupling constants, corresponding to repulsive contact interactions on the Bloch sphere. In this situation, the minimization of energy is equivalent to the Thomson problem of the equilibrium position of $2J$ charged particles constrained to a sphere [37]. We show in Fig. 1.14a the ground-state vortex configuration for $J = 8$. The vortices are regularly dispatched over the sphere, reminding the triangular Abrikosov lattice on the infinite plane.

For smaller atom numbers $N \sim 2J$, the system should form complex many-body states akin to fractional quantum Hall states. In particular, the bosonic Laughlin state for $N = J + 1 = 9$ particles is the exact ground state for contact interactions (see

[†] The position shift comes together with an energy offset proportional to m, that can be compensated by a magnetic field producing an opposite Zeeman shift.

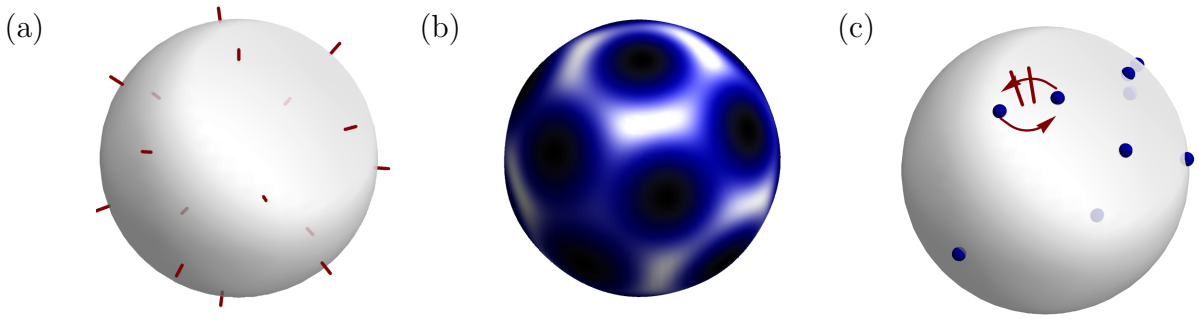

Figure 1.14: (a) Positions of the $2J$ vortices for the mean-field ground state with repulsive contact interactions on the Bloch sphere. (b) Corresponding Husimi function with holes at the vortex positions. (c) Schematics of the Laughlin liquid expected at filling 1/2, for a set of 9 atoms. Each atom carries a collective spin J (blue dots) delocalized over the Bloch sphere. In the Laughlin state, atom pairs exhibit a double vortex in their relative spin motion.

Fig. 1.14a) [38]. Exploring this very rich physics requires specific experimental protocols based on the manipulation of mesoscopic atomic samples.

2 Artificial quantum Hall systems

The high degree of control reached in ultracold atom experiments makes these systems relevant for the quantum simulation of complex models of quantum many-body physics. While the control over dimensionality and (short-range) interactions is well established, the simulation of artificial gauge fields remains a challenge.

Soon after the first realization of Bose-Einstein condensates, orbital magnetic field effects were simulated by setting the gases in rotation [39], based on the analogy between the Sagnac phase of a particle in a rotating frame and the Aharonov-Bohm phase of a charged particle in a magnetic field. The superfluid character of Bose-Einstein condensates entails the quantization of vorticity. Condensates in rotating traps then exhibit a regular array of quantized vortices, akin to Abrikosov lattices in rotating liquid helium or type-II superconductors in a magnetic field [39, 40]. In harmonically trapped gases, an interesting regime is reached when the rotation frequency Ω matches the confinement frequency ω, as the single-particle eigenstates become formally equivalent to the Landau levels of a charged particle evolving in a magnetic field [41]. Several experiments could reach the regime in which the gas dynamics is restricted to the Lowest Landau level (LLL) [42, 43], similarly to quantum Hall systems realized in condensed matter physics, using quantum wells or monolayer materials. So far, rotating gases could be understood in a mean-field description, where the number of particles N largely exceeds the number of occupied single-particle orbitals ('number of fluxes' N_ϕ). For a filling fraction N/N_ϕ of order one, one expects strongly-correlated ground states, similar to fractional quantum Hall states [41]. Reaching this regime is challenging in rotating systems, as it occurs at very small atom densities and temperatures.

Other techniques were developed to circumvent the limits encountered in rotating gases and simulate more complex gauge fields (e.g. an effective spin-orbit coupling) [44]. The first protocol consists in applying to the atoms a position-dependent coupling to their internal spin. The adiabatic motion of an atom in the local ground state comes together with a geometrical Berry phase [45], which can mimic the Aharonov-Bohm phase associated with a magnetic field. Such a spatial variation of adiabatic states can be achieved down to the micron scale by coupling the spin to laser fields [46]. This scheme was implemented with Rb atoms, allowing the nucleation of quantized vortices [47]. Nevertheless, residual incoherent scattering from the coupling lasers induce heating of the atomic gas, preventing the organization of vortices into an Abrikosov lattice. The second technique consists in placing the atoms in an optical lattice, in a Hubbard regime where the atom dynamics is described on a discrete lattice [48]. There, a non-trivial Aharonov-Bohm phase corresponds to complex-valued hopping amplitudes between lattice sites [49]. Such effective couplings were realized in time-modulated optical lattices [50]. A quantum Hall regime is reached when the atomic gas fills a Bloch band exhibiting a non-trivial topological character, such as a Chern number $\mathcal{C} = 1$ akin to the LLL [51, 52]. This protocol was extended to systems in which a spatial dimension is encoded in an internal spin degree of

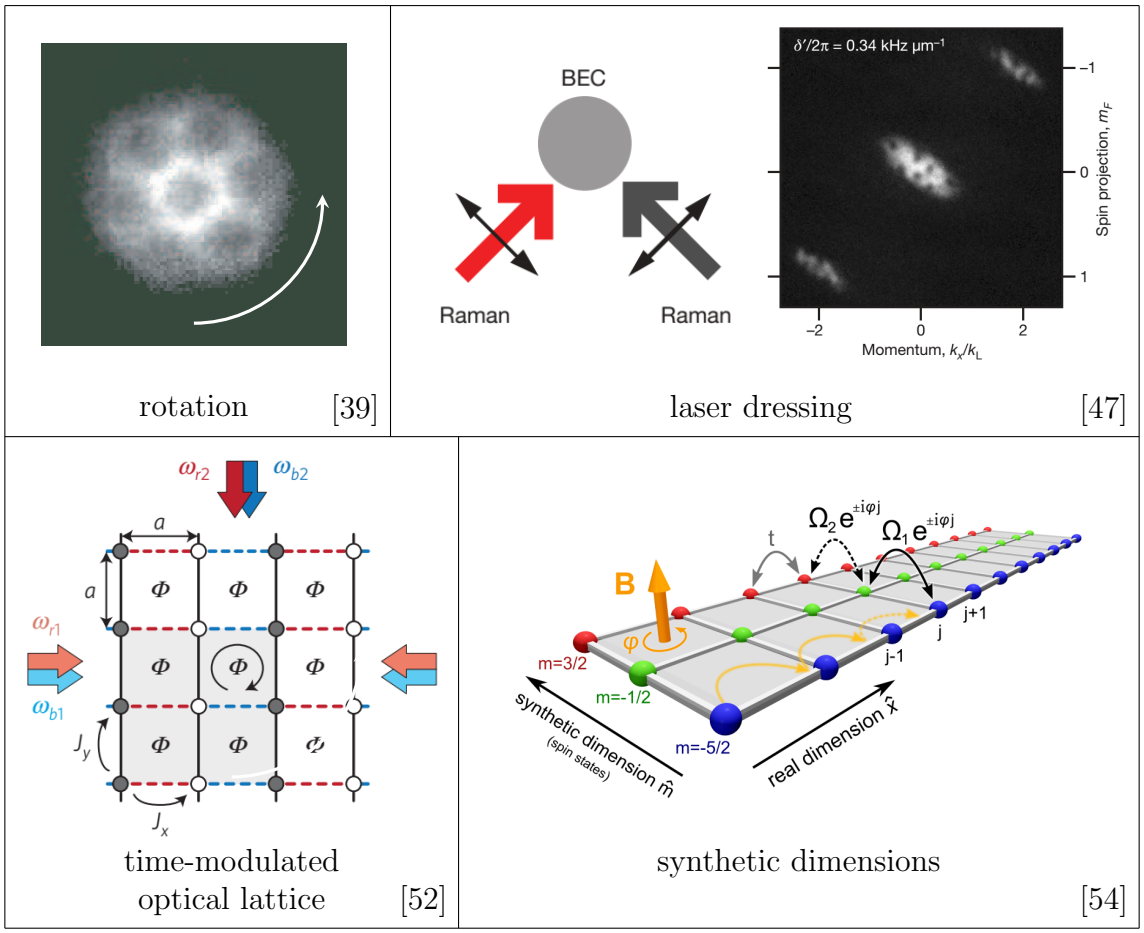

Figure 2.1: Schematics of the four types of protocols developed to engineer an orbital magnetic field for ultracold atoms. This manuscript describes contributions to the development of time-modulated lattices and synthetic dimensions.

freedom [53, 54, 55]. This protocol is well adapted to study topological edge modes, since the finite synthetic dimension features sharps boundaries.

In this chapter we describe two experimental studies on the realization of quantum Hall systems with ultracold atoms. We first describe experiments performed in the Munich group, on the engineering of complex-valued tunneling amplitudes in an optical lattice [50]. We demonstrated the quantization of the transverse response of atoms placed in a topological Bloch band [52]. More recently, we engineered a quantum Hall system in cold dysprosium gases, taking advantage of the large electronic spin $J = 8$, playing the role of an effective spatial dimension [56]. Combined with a non-trivial dynamics involving a real spatial dimension, we could implement an effective two-dimensional system analog to the LLL. We revealed both the quantization of the transverse response of the system in its bulk, and observed the topologically protected chiral modes at the system edges.

2.1 Topological bands in driven optical lattices

During my postdoctoral stay in the group of Prof. I. Bloch (Munich, Germany), we have investigated the simulation of orbital magnetism in optical lattices, based on fast time

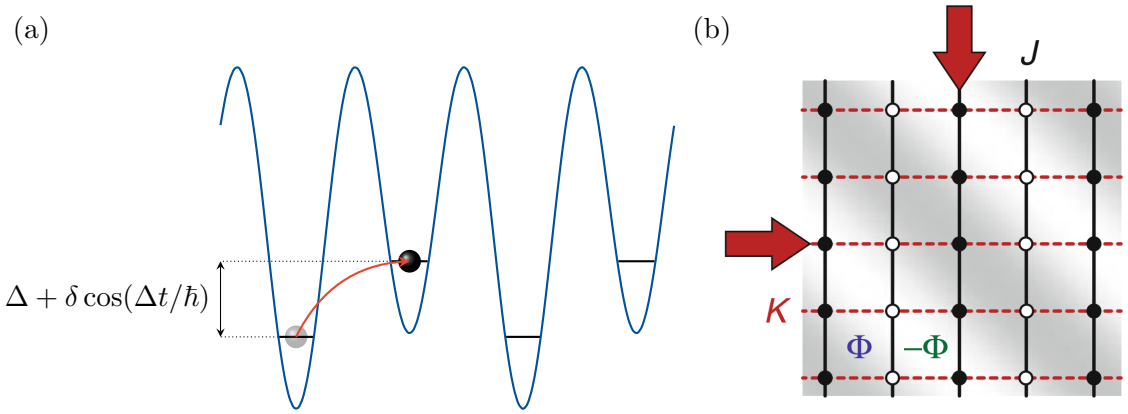

Figure 2.2: (a) Scheme of atom tunneling between lattice sites of different energy Δ. A modulation of the energy offset at the frequency $\Delta/\hbar$ drives resonant tunneling. (b) In a two-dimensional lattice, a time modulation induced by interfering laser beams leads to effective atom tunneling with non-trivial complex matrix elements. In its most basic scheme, this technique leads to a magnetic flux that alternates in sign [50] (adapted from [57]).

modulation of the lattice potential.

By varying the geometrical configuration of optical standing waves, one can engineer various types of lattice potentials, from the simple cubic lattice to hexagonal of Kagomé lattices, with a large variety of band structures. In these static lattices, the atom motion is described by real and positive tunneling amplitudes. Engineering effective tunneling amplitudes with a negative sign or even with complex values gives access to an even richer family of lattice structures, in which the atom motion is geometrically frustrated.

Such a control over the tunneling amplitudes can be achieved in time-modulated optical lattices [58]. We show in Fig. 2.2a a basic scheme, based on a lattice structure with two inequivalent lattice sites of different energies, such that spontaneous atom tunneling is prohibited. By modulating their energy difference, one restores tunneling when the modulation frequency matches the mean energy difference Δ. The effective tunneling amplitude being proportional to the potential modulation, a non-trivial structure arises when the phase of the modulation varies in space, such that the complex tunneling amplitudes cannot be gauged away. In that case, the adiabatic motion of an atom around an elementary unit cell of the lattice occurs together with the accumulation of a geometric Berry phase, equivalent to the action of an orbital magnetic field.

A regime of strong orbital magnetic fields can be reached when the hopping is stimulated by the absorption of photons [59, 60]. In such a configuration, one unit of magnetic flux is reached over an area $\sim \lambda^2$, i.e. comparable to the lattice unit cell. The resulting band structure is split in several subbands, as described by the Harper-Hofstadter butterfly [61, 62].

In the Munich experiment, we studied the dynamics of cold atoms evolving in an optical superlattice, with an alternance of two lattice sites of different energies. We first induced the dynamics using a simple modulation $\propto \cos(\mathbf{K}\cdot\mathbf{r} - \Delta t)$, for which the orbital magnetic field alternates in sign (see Fig. 2.2b). The geometrical frustration induced by the magnetic field modifies the dispersion relation, eventually leading to a degeneracy of the single-particle ground state [50].

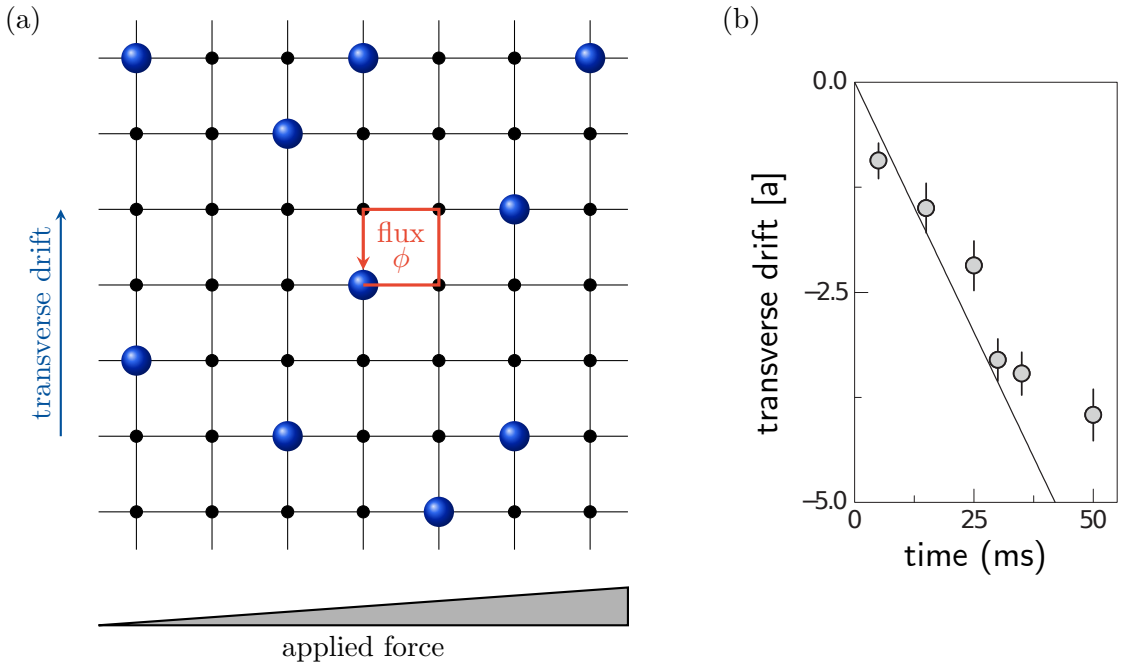

Figure 2.3: (a) Scheme of the Hofstadter lattice realized in the Munich experiment, with a magnetic flux per plaquette $\phi = \pi/2$. The Chern number of the lowest magnetic Bloch band is probed via the transverse drift of the atoms upon an external force. (b) Measured transverse drift of the center of mass (gray circles), together with the expect drift for a Chern number $\mathcal{C} = 1$ (solid line). Adapted from [52].

We extended this technique to a more complex modulation pattern, allowing us to generate a uniform magnetic flux of $\pi/2$ per unit cell of the underlying lattice [52]. In this configuration, the band structure splits into four subbands, with a lowest band characterized by a non-zero Chern number $\mathcal{C} = 1$. By analogy with the quantization of the Hall conductance in 2D electron gases, we revealed this topological number via the transverse response of the atomic gas to a weak force (see Fig. 2.3a). More precisely, we prepared a thermal gas filling uniformly the lowest magnetic Bloch band, and measured the drift of the center of mass along y induced by upon a weak force along x. We found that, when the action of the force corresponds to one Bloch oscillation cycle along x, the system has drifted by one lattice spacing along y, as expected for a Chern number $\mathcal{C} = 1$ (see Fig. 2.3b).

These studies, together with other periodically driven systems, demonstrate the versatility of Floquet engineering to produce complex band structures [63, 64]. Nevertheless, the exploration of topological quantum matter in these systems remains challenging, due to relatively high heating rates so far preventing the creation of quantum degenerate phases. This detrimental heating takes its origin in the unbounded energy spectrum of Floquet systems, allowing for a large number of 'inelastic' processes [65, 66, 67, 68]. It could be mitigated by coupling the atomic gas to a superfluid reservoir [69], or increasing the modulation energy scale to optical frequencies [70].

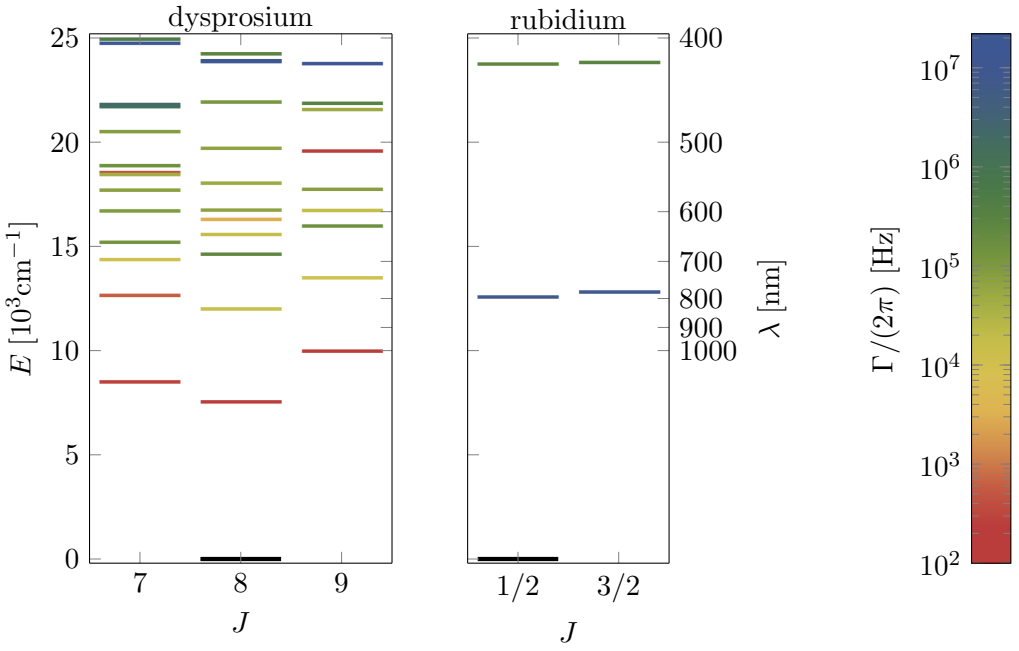

Figure 2.4: Electronic spectrum of atomic dysprosium and rubidium, restricted to the electronic ground state (black line) and the odd-parity excited states of energy $E < 25\,000\,\mathrm{cm}^{-1}$. The color encodes the excited-state lifetime.

2.2 Landau levels in atomic Dysprosium

2.2.1 New physical regimes using lanthanide atoms

The condensation of dysprosium and erbium in 2011 and 2012 brought new perspectives in the cold atom community [71, 72]. Besides their large magnetic moment, these submerged-shell lanthanide atoms feature physical properties appealing for the generation of artificial gauge fields [73].

A first asset of dysprosium (or erbium) is the strong coupling of its electronic spin to laser fields, as required to generate gauge fields in adiabatic potentials. A light-spin coupling occurs when shining laser light close to an optical resonance connecting the electronic ground state J to an excited level J', according to the corresponding Clebsch-Gordan algebra. The laser detuning must be chosen small enough for the considered optical transition to dominate with respect to other transitions, and large enough to reduce the incoherent Rayleigh scattering that mechanically heats up the gas. In alkali atoms, the D_1 and D_2 lines are relatively broad compared to their (fine-structure) splitting, such that light-spin coupling comes together with a substantial heating [47]. The situation is more favorable for lanthanide atoms, which exhibit a rich electronic structure with isolated and narrow optical transitions.

A second interesting characteristics of lanthanide atoms is their large electronic angular momentum, providing an internal degree of freedom of large dimension. The latter can be used to encode a synthetic spatial dimension, which greatly facilitates the generation of a gauge field. So far gauge fields with a synthetic dimension were restricted to a few internal states only [54, 55]. We discuss in this section an experimental study in which we generated a gauge field using the full spin degree of freedom of dysprosium, i.e. a

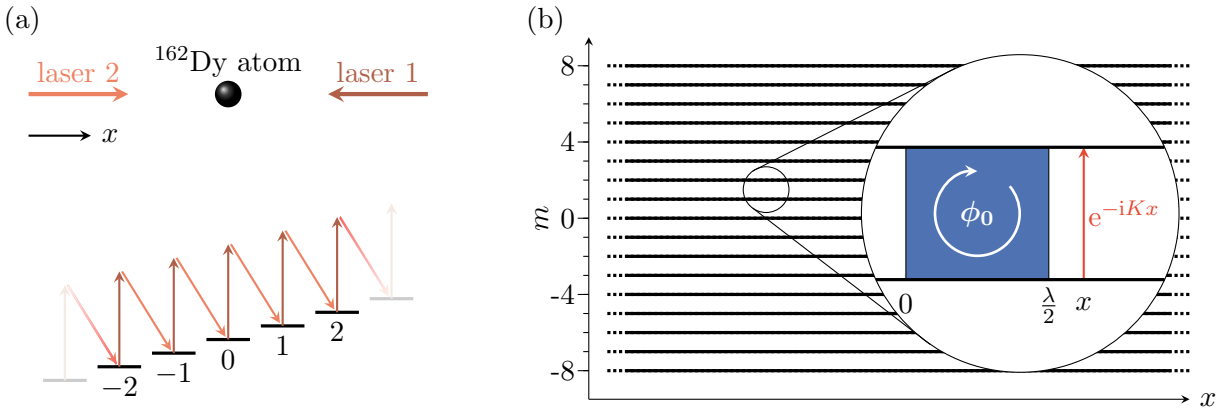

Figure 2.5: (a) Scheme of the laser configuration used to engineer effective Landau levels with a synthetic dimension. A pair of laser beams counter-propagating along x drives two-photon Raman transitions between successive projection states m. (b) Scheme of the two-dimensional system involving a spatial dimension x and a synthetic dimension m. The laser-induced hopping along m inherits the complex phase Kx of the Raman laser interference. This phase can be interpreted as the Aharonov-Bohm phase acquired by a charged particle upon adiabatic motion in a magnetic field. The blue area is thread by one unit of magnetic flux ϕ_0.

synthetic dimension made of $2J + 1 = 17$ orthogonal quantum states [56]. We showed that the synthetic dimension is large enough to allow for a uniform bulk region. We revealed, in a single experiment, the existence of chiral edge modes and a quantized Hall response in the bulk – the two facets of the bulk-boundary correspondence of topological physical systems [74].

2.2.2 Implementing a Hall ribbon with a synthetic dimension

We engineered a synthetic Hall system in which the relevant atom dynamics involves one spatial dimension x and a synthetic dimension indexed by the spin projection m ($-J \leq m \leq J$) along a quantization axis. Our implementation is directly inspired by previous realizations using ^{87}Rb and ^{173}Yb [54, 55]. The protocol is schematized in Fig. 2.5. By coupling successive m states with two-photon Raman transitions, we induce a hopping along the synthetic dimension whose amplitude inherits the complex phase Kx of the laser interference. This phase plays the role of a Aharonov-Bohm phase, such that the atom dynamics is described by a Hamiltonian

$$\hat{H} = \frac{(\hat{p} - \hbar K \hat{J}_z)^2}{2M} - \hbar\Omega \left(\hat{J}_x + \frac{\hat{J}_z^2}{2J+3} \right) \tag{2.1}$$

with an effective gauge field $\hat{A} = \hbar K \hat{J}_z$. Once the spin projection $\hat{J}_z$ is identified with the position along the synthetic dimension, the gauge field $\hbar K \hat{J}_z$ can be mapped on the expression $\hat{A}_x = qB\hat{y}$ of a charged particle in a magnetic field, expressed in the Landau gauge. The flux of the effective magnetic field reaches one flux quantum over an area $(\lambda/2) \times 1$ in the real $\times$ synthetic plane.

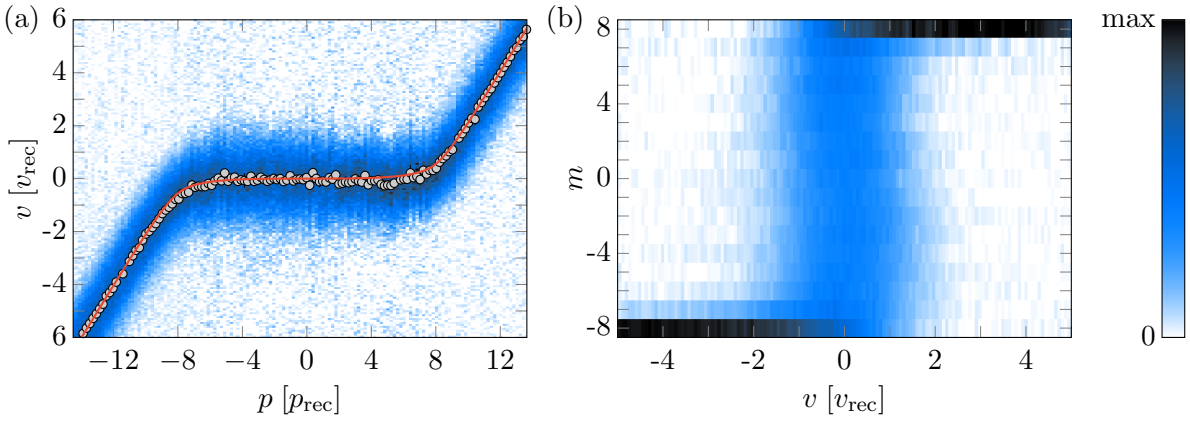

Figure 2.6: (a) Measured velocity distribution of ground-band states of momentum p. The gray dots correspond to the mean velocity $\langle v \rangle$. The red line is the expected mean velocity for the ground band of the Hamiltonian (2.1) (b) Local density of state in (v, m) space, obtained by summing the spin projection and velocity distributions of all momentum states of the ground band.

2.2.3 Observation of a flat band with chiral edge modes

We studied the lowest energy band by preparing and probing quantum states of the ground band of the Hamiltonian (2.1) with a given momentum p. For each momentum state, we measured its velocity distribution (see Fig. 2.6a) and spin projection probabilities. The correlation between these two quantities, shown in Fig. 2.6b, is characteristic of a quantum Hall system. In the bulk (i.e. far from the edges $m = \pm J$), the velocity is suppressed, revealing an absence of energy dispersion in the ground band, akin to dispersionless Landau levels. Close to the edges, we find that the motion is ballistic, albeit with a restriction $v > 0$ close to $m = J$ (and vice versa), as expected for chiral edge modes.

We also investigated the low-energy excitations above the ground band, by monitoring the center-of-mass motion after a small kick (see Fig. 2.7a). In the bulk, we measure circular orbits reminiscent of a cyclotron motion. Close to the edges, the trajectories acquire an additional drift, leading to bouncing skipping orbits. The frequency of these oscillations corresponds to the energy gap with respect to the first excited band, $\hbar\Delta \simeq 3E_{\mathrm{r}} \simeq k_{\mathrm{B}} \times 2\,\mu\mathrm{K}$ (see Fig. 2.7b). Such a value is a large energy scale for a quantum gas, compared to the temperatures $T \sim 100\,\mathrm{nK}$ typically required to reach quantum degeneracy. This feature is a clear asset of our scheme for future studies of quantum gases in the presence of a synthetic gauge field.

2.2.4 Probing the topological Hall response

We characterized the Hall response of the system by studying the transverse motion induced by a weak force (see Fig. 2.8a). We applied the force along the synthetic dimension, corresponding to a potential difference $U = 2J\delta$ between the two edges $m = \pm J$. We measured the increase of velocity $\langle v \rangle$ along the real direction x, as

$$\langle v \rangle = \mu_{\mathrm{H}}\, \delta,$$

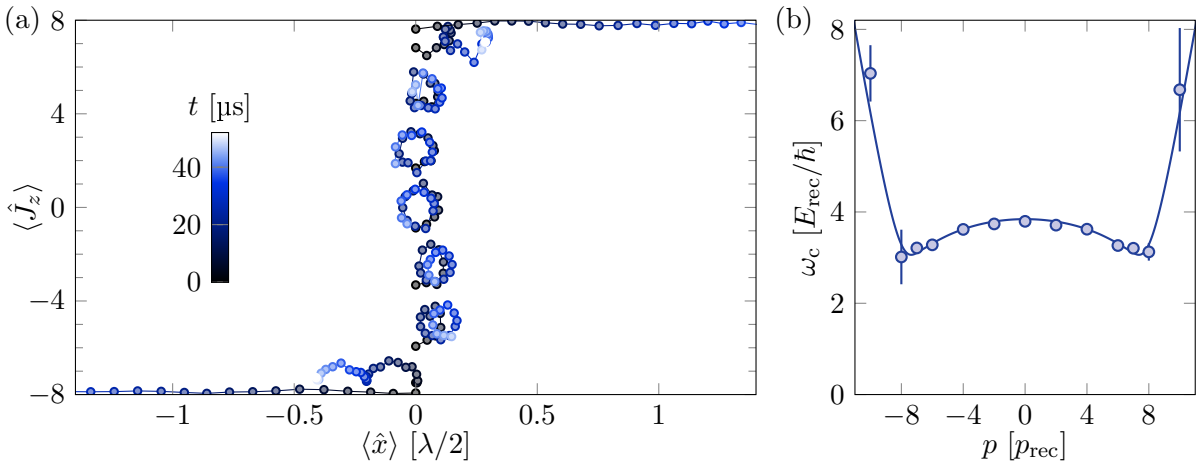

Figure 2.7: (a) Evolution of the center-of-mass position following a velocity kick along x. For each orbit the system is prepared in a wavepacket centered on a given momentum p, before the kick is applied. (b) Cyclotron frequency gap between the ground and first excited bands, as a function of the momentum p. The frequencies are measured from the center-of-mass oscillations shown in (a).

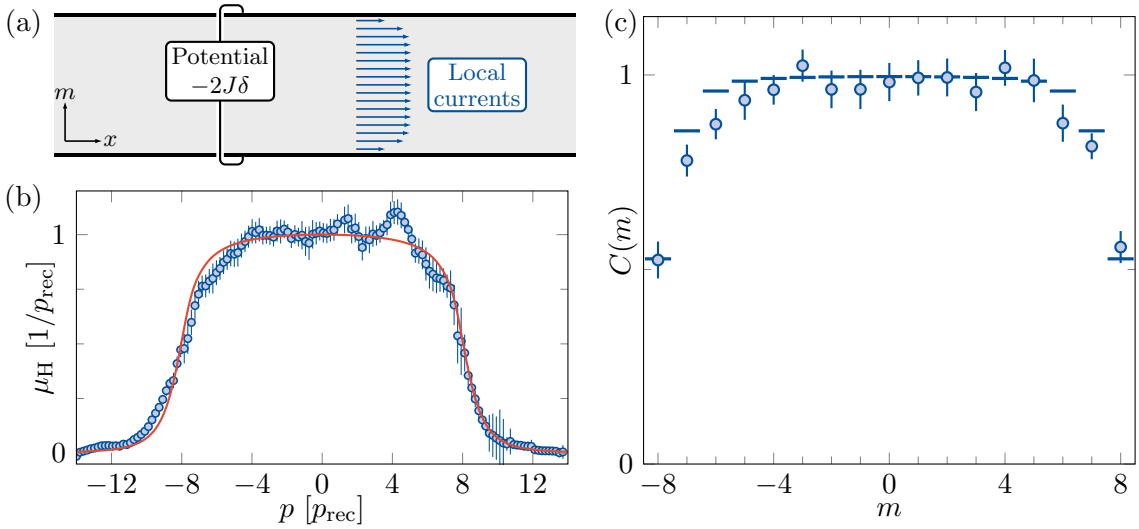

Figure 2.8: (a) Scheme of the Hall response measurement. (b) Hall mobility measured for wavepackets localized around a momentum p (blue dots), compared to the expected mobility (red line). (c) Local Chern marker $C(m)$ measured over the ground band (blue dots). The solid lines correspond to the theoretical values.

where the coefficient μ_H is the Hall mobility. The Hall mobility data is consistent with the classical Hall mobility $\mu_H = 1/\hbar K$ for momentum states localized in the bulk (see Fig. 2.8b). Conversely, it is suppressed for high-velocity ballistic states, which essentially do not feel the orbital magnetic field.

The m-state resolution allows us to locally probe this Hall response. We focused on the m-resolved global response of the ground band, described by the local Chern marker

$$C(x,m) \equiv 2\pi \,\mathrm{Im}\,\langle x,m|\,[\hat{P}\hat{x}\hat{P}, \hat{P}\hat{J}_z\hat{P}]\,|x,m\rangle\,,$$

where $\hat{P}$ is the projector on the considered band [75]. It can be expressed as the sum of the mobilities of the occupied states, weighted by their probability to be localized in m, as

$$C(m) = \int \mathrm{d}p\, \Pi_m(p)\mu_{\mathrm{H}}(p).$$

We show in Fig. 2.8c the measured Chern markers, which are consistent with one in the bulk region $-5 \leq m \leq 5$. In this region, edge effects are negligible, and the transverse response of the band is almost quantized and consistent with the topological Chern index $\mathcal{C} = 1$ expected for an infinite Landau level.

To summarize our results, we were able to engineer a quantum Hall system using a synthetic dimension large enough to exhibit both sharp edge effects and a well-defined bulk region. Our study could reveal the two facets of the bulk-edge correspondence inherent to any topological physical system.

2.3 Outlook: more complex topological systems

The synthetic dimension encoded in the electronic spin of dysprosium could be used to engineer more complex topological systems. We discuss here two examples, namely a two-dimensional system exhibiting a ground band with a Chern number $\mathcal{C} = 2$, and a three-dimensional topological insulator.

2.3.1 Band with a Chern number $\mathcal{C} = 2$

Our understanding of the fractional quantum Hall effect is based on the structure of single-particle quantum states organized in Landau levels, which are bands of Chern number $\mathcal{C} = 1$ separated in energy. Flat bands with a higher Chern number $\mathcal{C} = 2$ are expected to host novel topological phases [76, 77, 78], some of them being related to the rich phenomenology of bilayer quantum Hall systems [79].

A system exhibiting such exotic bands can be engineered using a protocol similar to the one used to generate effective Landau levels. Instead of coupling neighbouring projection states $m \leftrightarrow m \pm 1$ using σ_+/π or π/σ_- Raman transitions, one can directly couple next-nearest neighbours projection states $m \leftrightarrow m \pm 2$ using a σ_+/σ_- transition. For the configuration shown in Fig. 2.9a, the atom dynamics is described by a Hamiltonian

$$H = \frac{(p - \hbar k J_z)^2}{2M} + \hbar\Omega J_x^2 + q J_z^2, \tag{2.2}$$

involving a non-linear coupling J_x^2. The spin projection parity $(-1)^m$ is conserved, such that the dispersion relation consists in bands of well defined parity. The lowest energy bands of each parity sector are almost degenerate in the bulk, and globaly form an effective band of Chern number $\mathcal{C} = 2$. They share similarities with the lowest and first excited Landau levels, each obtained by suitable combinations of the two quasi-degenerate parity sectors. A truly novel physics is expected when considering interacting atoms in this structure, such that the interaction energy scale exceeds the residual splitting between the two lowest bands, and remains smaller than the gap to higher bands.

2.3.2 Topological insulator using a synthetic dimension

The electronic spin can also serve as a synthetic dimension to engineer a three-dimensional topological insulator based on a two-dimensional lattice structure. Topological insulators

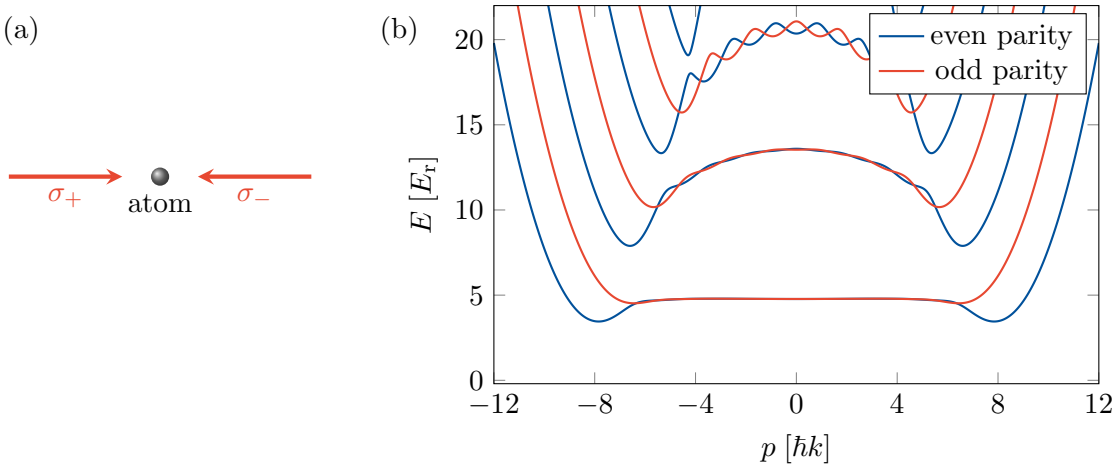

Figure 2.9: (a) Scheme of the laser configuration leading to a dynamics described by the Hamiltonian (2.2). (b) Dispersion relation calculated for the Hamiltonian (2.2) with $\hbar\Omega = 0.35\,E_r$ and $q = 0.04\,E_r$. The even- and odd-m sectors are uncoupled and represented in blue and red, respectively. The ground bands for each sector are almost degenerate in the bulk mode region $|p| \lesssim J\hbar k$, forming an effective band with Chern number $\mathcal{C} = 2$.

are three-dimensional physical systems with a non-trivial topological band structure, described by a bulk $\mathbb{Z}_2$ topological invariant [80, 81, 82]. In a finite sample, the topology manifests via the presence of protected surface states with peculiar properties: the two-dimensional dynamics on a given surface corresponds to a 'topological metal', with a dispersion relation hosting a single Dirac cone.

To date, several types of topological systems were realized in one and two dimensions using ultracold atoms [83]. In three dimensions, nodal-line and Weyl semimetals were recently created in atomic systems [84, 85], but the realization of topological insulators is still lacking, despite the existence of a proposal [86].

We show here a minimal protocol leading to a topological insulator using the electronic spin as a synthetic dimension. We use a spin-independent optical lattice in two spatial dimensions to engineer, for each magnetic projection m, a dispersion relation with two Dirac cones K and K', as realized in [87] (see Fig. 2.10a). The successive m states are coupled using a Raman transition, with a momentum transfer precisely equal to the separation between the two Dirac cones. Each Dirac point is then coupled to another one, except the point K for $m = -J$ and K' for $m = J$. The resulting dispersion relation is shown in Fig. 2.10b. The coupling between pairs of Dirac cones opens an energy gap, such that one is left with two Dirac cones only, one on the surface $m = -J$ and the other one on $m = J$. This feature is characteristic of a semi-metallic behavior at each surface – the analog of chiral edge modes in quantum Hall systems. We could probe this structure by generalizing the band dispersion studies developed in the study of synthetic Landau levels. Measuring both the dispersion relation together with the magnetization would reveal the semi-metallic behavior of the surface states.

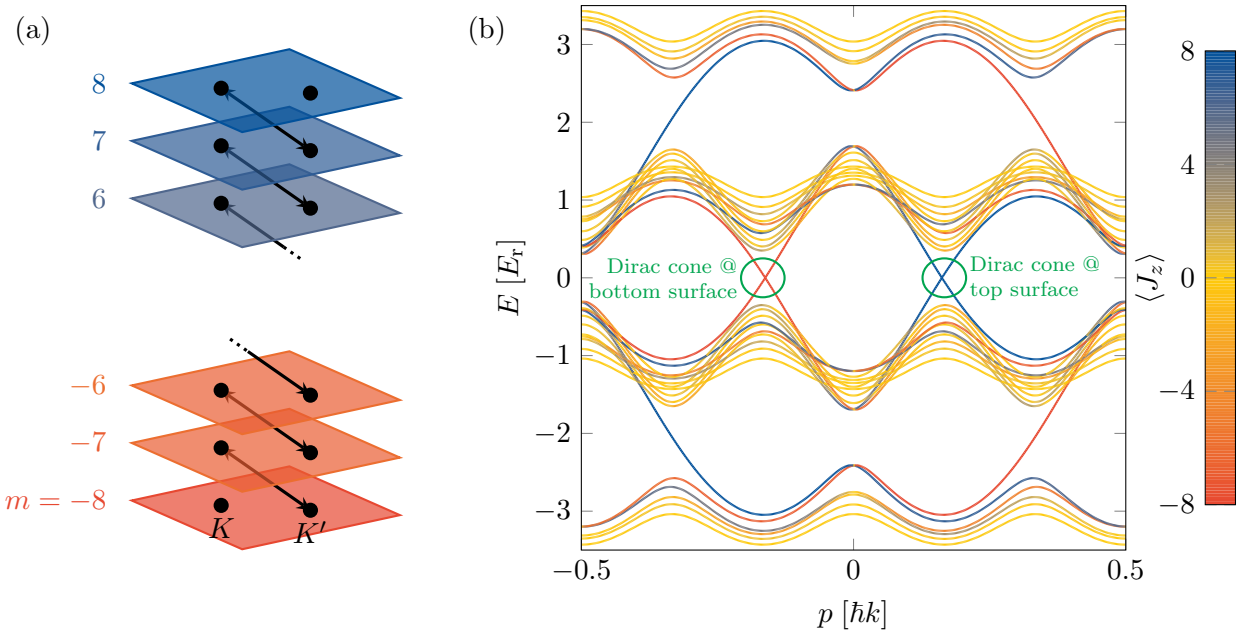

Figure 2.10: (a) Scheme of the protocol leading to a synthetic topological insulator. A two-dimensional optical lattice leads, for each magnetic projection m, to a band structure with two Dirac points (black dots). Successive m states are coupled with a two-photon laser transition imparting a momentum matching the difference in momentum between the Dirac points K and K'. Each Dirac point is coupled to another one, except the point K for $m = -J$ and K' for $m = J$. The color encodes the spin projection, i.e. the position along the synthetic dimension: blue close to the top surface $m = J$, red close to the bottom surface $m = -J$, yellow in the bulk. (b) Expected dispersion relation along the line connecting K and K'. The system is gapped around zero energy in the bulk (yellow lines), and each surface exhibits a single Dirac cone, spotted inside a green circle.

3 Towards topological quantum many-body systems

The engineering of topological band structures discussed in the previous section gives access to a subtle phenomenology, with a topological ordering of quantum states and exotic dynamics of edge modes. We stress that these behaviors only involve the structure of single-particle levels, and can be reproduced in many kinds of synthetic materials hosting similar linear wave dispersion [88]. A grand challenge consists in the extension of the concept of topology to interacting quantum many-body systems. Exotic states of matter have been discovered in the fractional quantum Hall effect, in the form of strongly correlated liquids hosting peculiar elementary excitations (e.g. anyons with a fractional quantum statistics). Our future scientific objectives are to contribute in the progress of ultracold atoms to the quest for these long-awaited states of matter.

We discuss here two research directions. We first consider interacting bosonic atoms in the presence of an orbital magnetic field, aiming at studying vortex lattices in a mean-field regime and fractional quantum Hall states for strong interactions. We also plan to study strongly-interacting fermions in the presence of a spin-orbit coupling, which could form a topological superfluid phase hosting Majorana bound states.

3.1 Quantum magnetism with bosonic atomic gases

In the second part of this manuscript we discussed the engineering of an orbital magnetic field, leading to a topological ordering of quantum states analogous to the integer quantum Hall effect. We plan to explore the behavior of interacting bosons in this structure, both in weakly- and strongly-interacting regimes.

3.1.1 Vortex lattices in a synthetic Hall ribbon

In a weakly interacting regime, ultracold bosons form a Bose-Einstein condensate at low temperature. Its velocity field being irrotational, the vorticity imposed by an orbital magnetic field occurs via the formation of singular quantized vortex lines, organized in a regular Abrikosov lattice. Such a behavior has been demonstrated in rotating Bose-Einstein condensates [39, 40], but its observation for laser-induced magnetic fields is still missing. We aim to use the Landau level structure based on a synthetic dimension to generate Abrikosov lattices of high vortex density.

Encoding a spatial dimension in the electronic spin strongly modifies interactions between atoms. We assume the dynamics to be restricted to one spatial dimension x and one synthetic dimension m. While the van der Waals interactions between atoms takes place at short distance along x, it occurs a priori between any combination of m levels.

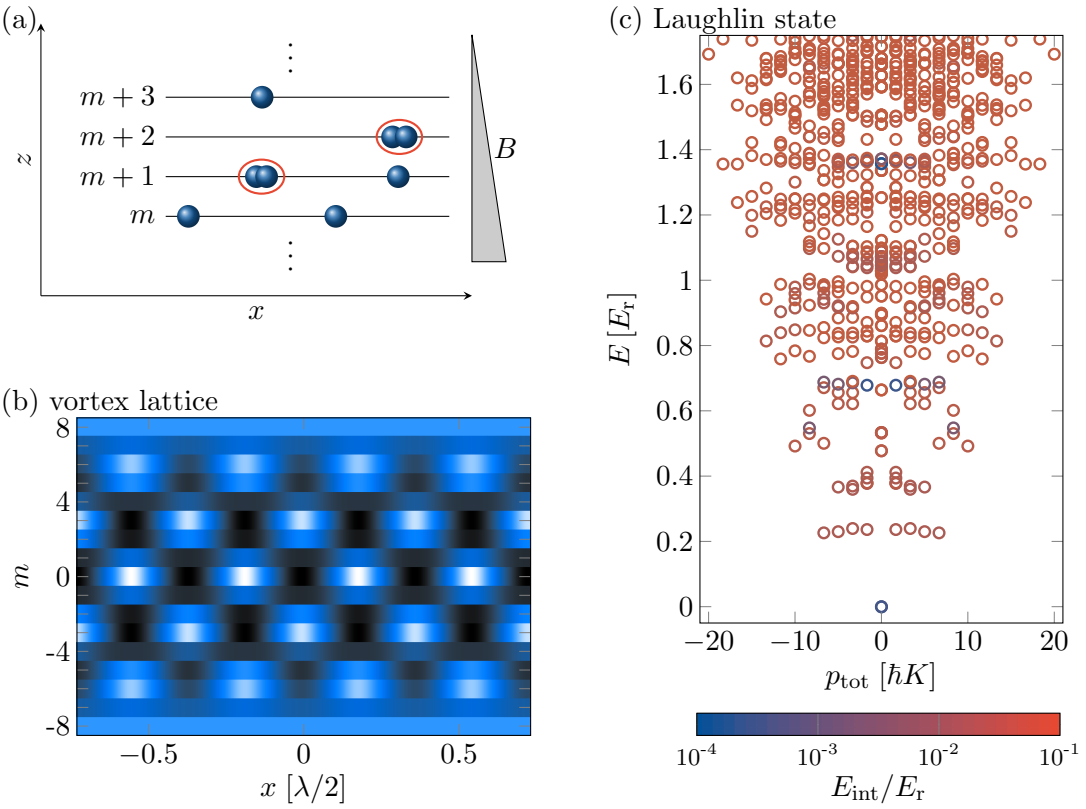

Figure 3.1: (a) Scheme of the protocol preventing collisions between atoms in different m states, by spatially separating them using a magnetic field gradient. The system is then governed by interactions of short range both in the real dimension x and the synthetic dimension m. (b) Typical density profile expected in the mean field regime. The continuous translation symmetry is spontaneously broken, and the system features regularly arranged density dips reminiscent of an Abrikosov lattice of quantum vortices. (c) Many-body spectrum expected in the strongly interacting regime, for $N = 5$ atoms in a finite cylinder. The length of the cylinder is chosen so as to populate $N_{\mathrm{orb}} = 9$ orbitals, corresponding to a filling 1/2. The ground state exhibits a very small interaction energy, as expected from the atom antibunching in the Laughlin state. It is well separated from higher levels by a bulk excitation gap $\hbar\delta \simeq 0.2\, E_{\mathrm{r}}$. Details on the system parameters can be found in [56].

In other words, its range along the synthetic dimension is infinite. This situation leads to specific states of matter, albeit different from the usual phenomenology of quantum Hall systems [89]. To circumvent this issue, we propose to use a magnetic field gradient to spatially separate the different m levels, restricting interactions to atom pairs in the same projection state m (see Fig. 3.1a). In this situation the collisions between atoms can be considered as short-ranged in both the real and synthetic dimensions*.

We first consider a regime of large atom densities, such that each quantum state of the lowest Landau level is occupied by many atoms ('large filling fraction'). At low

*Note that the direct interaction between magnetic dipoles is not negligible for dysprosium atoms. It leads to non-local interaction effects, but we do not expect a profound modification of the many-body phases discussed hereafter.

temperature, the system forms a Bose-Einstein condensate, which is well described by a classical field governed by the Gross-Pitaevskii equation. Since the bulk modes of the single-particle ground band are almost degenerate, interactions play a non-perturbative role, favoring the spreading of the atom density in case of repulsive interactions. We found numerically that the energy is minimized for a quantum superposition of several momentum states $p = n\,p_0$ (n integer), with a breaking of translation symmetry of spatial period h/p_0. As shown in Fig. 3.1b, the inhomogeneous density profile exhibits a regular pattern of density dips reminiscent of an Abrikosov vortex lattice. Similarly to type-II superconductor in confined geometries, different vortex lattice configurations can be realized, separated by first-order phase transitions.

3.1.2 Fractional quantum Hall states

In the weak density regime, the occupation of single-particle orbitals is of order one, such that a classical field picture is inapplicable. The many-body ground states then exhibit a complex pattern of correlations between atoms, leading to a rich phenomenology akin to the fractional quantum Hall effect. We discuss here the conditions leading to an emblematic many-particle ground state, the bosonic Laughlin state [90]. It occurs at filling $\nu = 1/2$, i.e. when the number of atoms is half the number of available orbitals [91].

The realization of such a state remains an outstanding challenge in the cold atom community. We believe that our system is a promising platform for its realization, based on two specific assets. First, the large vortex density in our system ($2J$ vortices per unit of $\lambda/2$) yields half filling at relatively high linear density $n_{1\mathrm{D}} = 2J/\lambda \simeq 25\,\mathrm{atoms/\mu m}$ – a value typically reached in quasi-1D bosonic gases [92]. Second, the cyclotron gap of our synthetic Landau levels is much larger than the values reached in rotating systems or in Hubbard optical lattices. This energy sets the scale of the maximum energy gap protecting the Laughlin state from bulk excitations [93]. The numerical simulation shown in Fig. 3.1c predicts a gap $\hbar\Delta \simeq 0.2\,E_\mathrm{r}$, corresponding to a temperature scale $\hbar\Delta/k_\mathrm{B} \simeq 100\,\mathrm{nK}$. This value is typical of the temperatures required to create a standard Bose-Einstein condensate.

This state could be characterized by observing an anti-bunching between atoms, due to the non-zero angular momentum in the relative motion of any pair of particles (Fig. 3.1c). The incompressibility could be revealed via a flat density profile in the presence of a weak trapping potential – similarly to the characterization of incompressible Mott phases in optical lattices [94]. The most exotic properties of fractional quantum Hall states, such as the anyonic character of its elementary excitations, would involve more complex protocols [95].

We mention an alternative protocol, that we studied in a previous publication [96]. We proposed to create small puddles of a few atoms in fractional quantum Hall states, by injecting a controlled amount of angular momentum to a mesoscopic atomic gas, based on optical transitions using Laguerre-Gauss laser beams. Atomic dysprosium is also well suited for this protocol, where we could benefit from the efficient light/spin coupling and the large electronic spin.

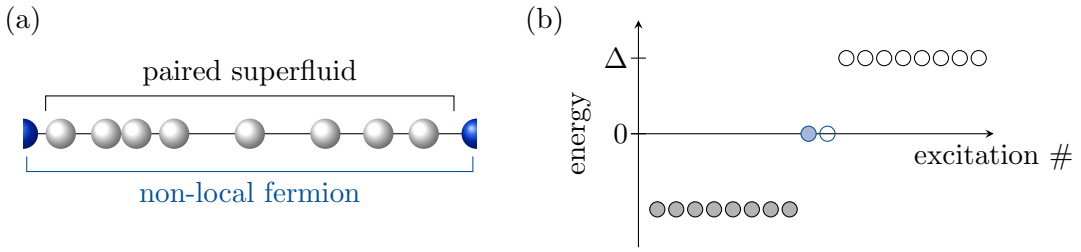

Figure 3.2: (a) Schematics of a p-wave superfluid with sharp ends, as described in the article of A.Y. Kitaev [99]. The particles are paired together in the bulk, and one expects an additional fermionic excitation delocalized between the two ends. (b) Expected energy spectrum of Kitaev's model, with bulk excitations suppressed by the superconducting gap, and a zero-energy excitation corresponding to the occupation of the fermionic end mode.

3.2 Topological superfluidity in spin-orbit coupled Fermi gases

We discuss in this section the perspective of realizing topological superfluids in interacting Fermi gases with a light-induced spin-orbit coupling. Topological superfluids are probably the most simple examples of interacting many-body systems exhibiting topologically protected modes – the so-called Majorana bound states or 'Majoranas' – with an anyonic quantum statistics. These projects are based on a published article [97], and a recent study, unpublished yet [98].

3.2.1 Topological superfluidity from solid-state to atomic systems

The occurrence of Majorana bound states was first predicted in a seminal article of A.Y. Kitaev [99], based on a one-dimensional superconductor of spin-polarized fermions with p-wave symmetry (see Fig. 3.2). Its lowest energy band exhibits a non-trivial topology, induced by the odd parity of the superconducting gap. In a finite system with open boundaries, one expects the occurrence of in-gap protected end states, described as Majoranas. A Majorana end state can be viewed as a bound state of a pair of distant Majorana fermions, equivalent to a non-local fermionic degree of freedom. In a more complex geometry (wire networks [100] or two-dimensional $p + \mathrm{i}p$ superconductor [101]) a set of Majoranas bound to topological defects forms a degenerate subspace of qubits that is decoupled from local perturbations. Quantum computing within this subspace can be performed via braiding operations, i.e. adiabatic manipulations of a Majorana defect around others [102]. Since Majorana modes are highly decoupled from the environment, such operations could be performed with a very low error probability, a prerequisite for scalable quantum computing [103].

Topological superconducting phases have been predicted in various types of platforms, including the fractional quantum Hall state at filling $\nu = 5/2$ [104, 101], the layered compound Sr_2RuO_4 [105], spin liquids [106], and engineered solid state systems [107, 108, 109]. The latter are based on the stacking of several materials combining different effects (e.g. ferromagnetism, spin-orbit coupling, superconductivity, topological insulation), that do not occur together in a single material. Several experiments have claimed the observation

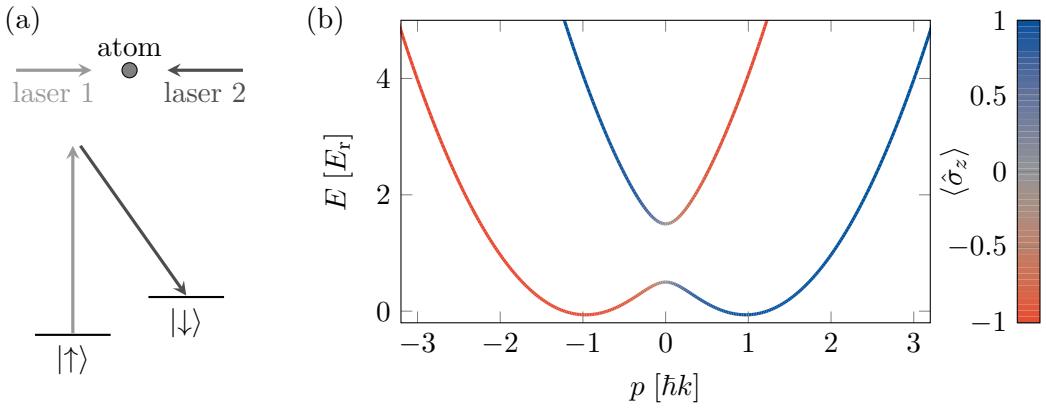

Figure 3.3: (a) Schematics of the laser configuration used to generate a spin-orbit coupling. A pair of counter-propagating laser beams coherently couples two internal states of an atom. (b) Dispersion relation of a spin-orbit coupled atom, as described by the Hamiltonian (3.1) with a coupling strength $\Omega = E_\mathrm{r}/\hbar$. The color encodes the mean spin projection along z.

of Majoranas, via the occurrence of robust in-gap states. However, the interpretation of these results remains debated, since they could also be induced by alternative effects. More demanding experiments, such as the manipulation of Majoranas and the realization of braiding operations, should be performed to provide a more conclusive proof of the realization of Majoranas.

In this context, ultracold atoms constitute an appealing alternative platform, with specific advantages, such as an intrinsic low disorder and a simple access to long-range coherence. The realization of a p-wave superfluid in a spin-polarized Fermi gas is not straightforward, due to the suppression of p-wave scattering at the ultracold energy scale. We discuss here the prospect of realizing a topological superfluid in a two-component Fermi gas, in the presence of a spin-orbit coupling and a Zeeman field.

3.2.2 Spin-orbit coupled Fermi gases

As first demonstrated by the seminal work of I. Spielman's group [110], spin-orbit coupling can be engineered in atomic gases by coupling two internal states of an atom with a two-photon optical transition (see Fig. 3.3a). Denoting $|\uparrow\rangle$ and $|\downarrow\rangle$ the two internal states and k the photon momentum, the single-particle dynamics is described by the Hamiltonian

$$\hat{H} = \frac{(\hat{p} - \hbar k \hat{\sigma}_z)^2}{2M} + \frac{\hbar\Omega}{2}\hat{\sigma}_x, \tag{3.1}$$

where Ω is the two-photon Rabi coupling amplitude. It involves a spin-orbit coupling between the spin component $\hat{\sigma}_z$ and the momentum $\hat{p}$, and a Zeeman coupling along $\hat{\sigma}_x$. The dispersion relation, shown in Fig. 3.3b, consists of two non-degenerate energy branches, with a momentum-dependent spin polarization. This structure was the framework of numerous studies of spin-orbit coupled Bose gases, which feature a specific behavior at low temperature due to the ground-state degeneracy at two different momenta [111].

Here, we are interested in the behavior of degenerate Fermi gases in the presence of spin-orbit coupling. First attempts were made with alkali atoms, but their unfavorable electronic level structure makes the light-spin coupling inefficient, and the realization

of spin-orbit coupling comes together with undesired heating of the atomic gas due to incoherent Rayleigh scattering [112, 113]. As already explained in this thesis, lanthanide atoms are better suited for laser-induced spin-orbit coupling, thanks to the strong light-spin coupling close to an isolated narrow optical transition. A first step was realized in the group of B. Lev [114], implementing spin-orbit coupling for fermionic dysprosium atoms. The atom lifetime was then limited by dipolar relaxation, due to the release of a large magnetic field splitting energy upon spin flips induced by dipolar interactions. We plan to implement spin-orbit coupling in the absence of an external magnetic field in order to suppress dipolar relaxation, expecting reduced atom heating as required for producing quantum degenerate Fermi gases.

The realization of topological superfluidity requires combining spin-orbit coupling and strong s-wave interactions. The scattering between atoms restricted to the ground band is then described by an odd-symmetric scattering amplitude. Assuming for simplicity the BCS approximation (collision between particles of opposite velocity), the dynamics restricted to the ground band is described by the Hamiltonian [115]

$$\hat{H} = \sum_p \epsilon_p \hat{c}_p^\dagger \hat{c}_p + \frac{1}{2} \sum_{p,p'} V_{p,p'} \hat{c}_{p'}^\dagger \hat{c}_{-p'}^\dagger \hat{c}_{-p} \hat{c}_p,$$
$$V_{p,p'} \simeq \frac{4\pi\hbar^2 a}{M} \operatorname{sgn}(p) \operatorname{sgn}(p'),$$

where $\hat{c}_p$ annihilates a particle of momentum p and energy ϵ_p in the ground band, and a is the s-wave scattering length for scattering of two atoms of opposite spin. We assumed the momenta p and p' to be close to the Fermi momentum p_F, with the Fermi energy E_F chosen in the avoided crossing at low momenta (e.g. $E_\mathrm{F} = E_\mathrm{r}$ for the dispersion shown in Fig. 3.3b). In that case, the ground-branch states are almost spin-polarized along z, the orientation being locked to the sign of the momentum. In a mean-field approximation, such a scattering gives rise to an odd-parity superfluid gap, and hence to topological superfluidity. In practice the interactions should be large enough to avoid the exponential suppression of the superfluid critical temperature. For a scattering length $|a| \sim \hbar/p_\mathrm{F}$ one expects a critical temperature comparable to the Fermi energy [116], as realized in conventional strongly-interacting Fermi gases [117]. This regime will be reached using a Fano-Feshbach resonance, or using a resonant enhancement of interactions using strong transverse confinement.

3.2.3 Signatures of Majoranas in atomic systems

In solid-state systems, quantum wires in a topological superconducting phase are coupled to a Cooper pair reservoir [118]. As shown in Fig. 3.4a, this system exhibits a topological degeneracy, with two degenerate ground states differing by the electron number parity. However, superselection rules forbid any sort of coupling between these states as long as the atom number parity is conserved. A more interesting situation occurs when the system exhibits four topological defects, e.g. in a pair of topological quantum wires. There, the ground state is four-fold degenerate, with a basis indexed by the parities of each subsystem, as $|\mathrm{even}, \mathrm{even}\rangle$, $|\mathrm{even}, \mathrm{odd}\rangle$, $|\mathrm{odd}, \mathrm{even}\rangle$ and $|\mathrm{odd}, \mathrm{odd}\rangle$. The total parity being conserved, the dynamics is restricted to a two-level system, for example $|\mathrm{even}, \mathrm{even}\rangle$ and $|\mathrm{odd}, \mathrm{odd}\rangle$, forming a topological qubit.

Contrary to electronic systems, atomic quantum wires are isolated from the environment and lack a superfluid reservoir. Then, a single wire hosts a non-degenerate

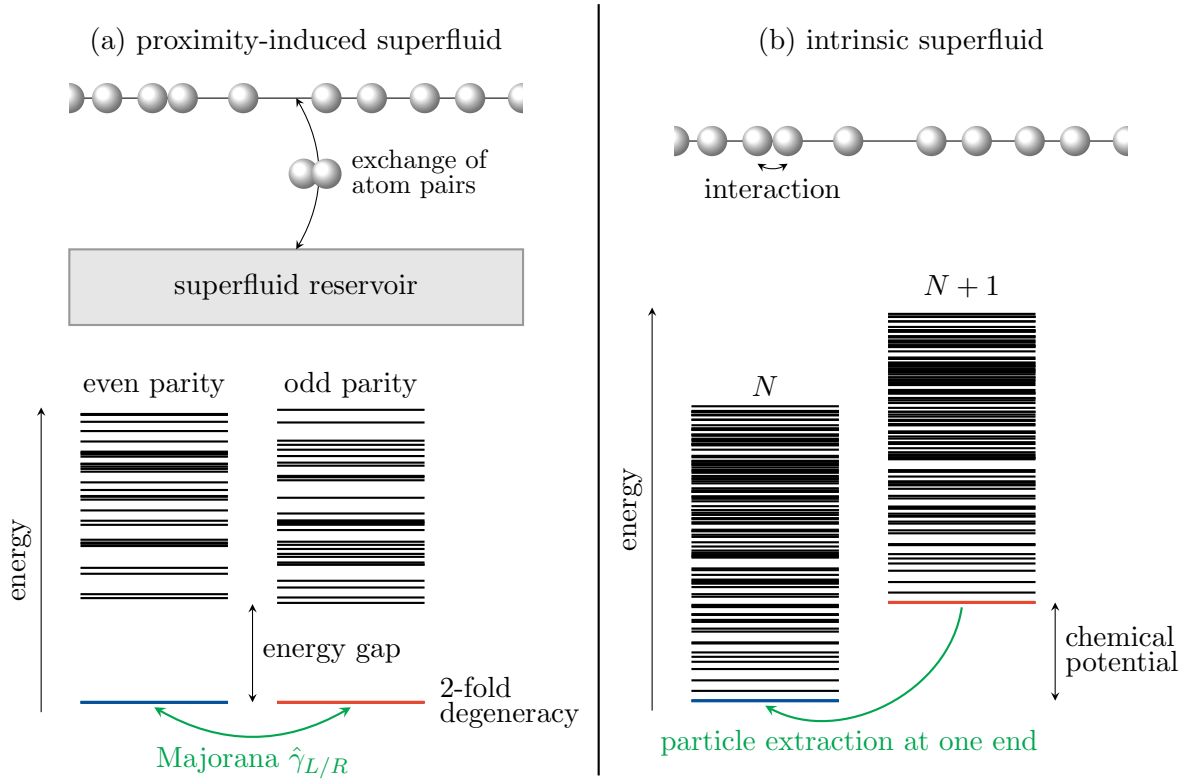

Figure 3.4: Comparison between the many-body spectra expected for single-wire topological superfluids. Superfluidity occurs from proximity to a superfluid reservoir in (a) and intrinsically from atom-atom interactions in (b). For a proximity-induced superfluid, long-range order of the superfluid reservoir grants a true energy gap protecting a two-fold degenerate ground state, one for each atom number parity. We stress that the conservation of parity prevents any coupling between these ground states, such that they cannot play the role of a topological qubit as such. An intrinsic superfluid with a conserved atom number N possesses a unique ground state, with gapless low-energy excitations in the thermodynamic limit. In both cases, Majorana-like correlations are revealed when extracting/adding a particle at the system ends.

ground state (see Fig. 3.4b). Topologically protected ground-state degeneracy requires a minimal system of two coupled atomic wires [119, 120, 121] – similarly to the minimal electronic system hosting a topological qubit. Isolated quantum wires, in which the superfluid character is 'intrinsic', show another important difference with electronic systems coupled to a BCS reservoir: their spectrum includes gapless phonon-like modes, preventing long-range order. Fortunately, one still expects a meaningful quasi-topological order [122, 123, 124, 125]. We mention that long-ranged ordered pairing can also be induced by coupling the atomic wire to a large superfluid system, in analogy with proximity-induced superconductivity [126, 97].

Several characteristics of Majoranas can be accessed in a single atomic wire. Indeed, the ground states for atom numbers N and $N+1$ can be coupled by extracting an atom of energy $\mu = E_0(N+1) - E_0(N)$ – an analog of photoemission spectroscopy in electronic systems. The extracted atom shares the characteristics of the Majorana end mode expected in the equivalent system connected to a superfluid reservoir: density localized at the system ends, with the phase difference between both ends locked to the

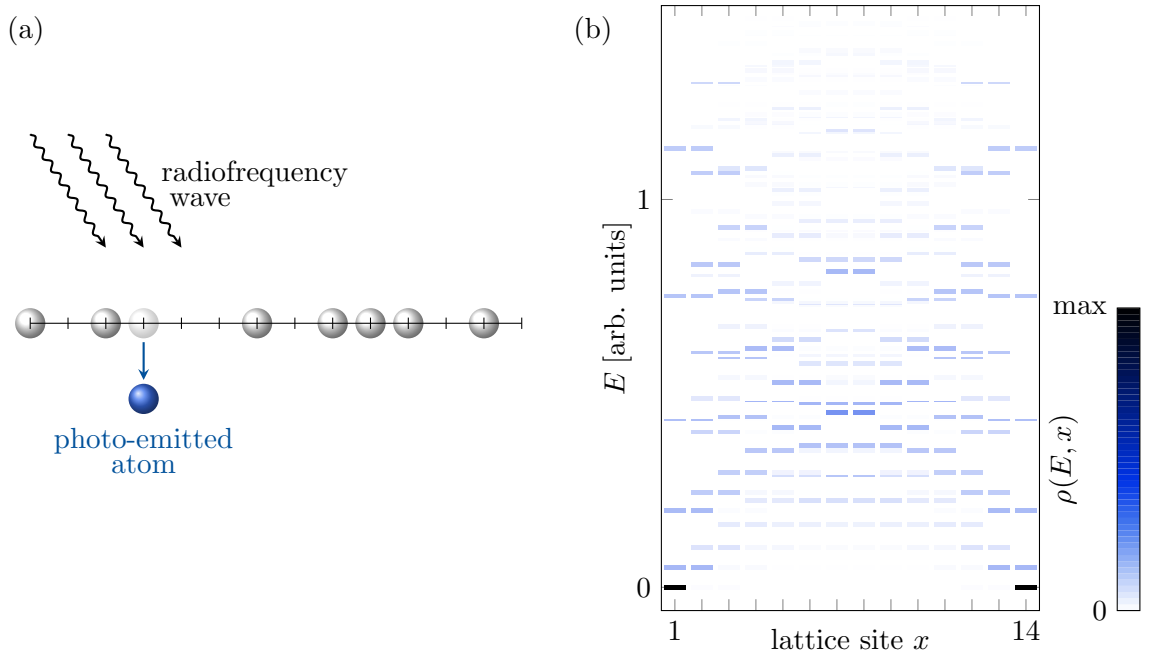

Figure 3.5: (a) Schematics of the photoemission experiment. A radiofrequency wave drives a transition towards an initially empty internal spin state. Starting in the many-body ground state with $N+1$ atoms, the transfer resonances give access to the excitation spectrum of the system with N atoms. The density distribution of these excitations can be accessed from the position of the atom extraction. (b) Expected excitation spectrum resolved in position, for an atom number $N = 7$ in a lattice of $L = 14$ sites. The zero-energy excitation occurs at the ends of the system, corresponding to a Majorana-like excitation.

parity of the atom number N.

We discuss in more detail the expected measurements using a toy model of a spin-polarized Fermi gas in a lattice, with extended interactions between nearest neighbours. This discussion is inspired by a previous project performed in collaboration with J. Dalibard, C. Mora and L. Mazza [98]. The ground state of this number-conserving model, originally introduced in [127], corresponds to the ground state of Kitaev's model projected on a fixed atom number N. We show in Fig. 3.5b the low-energy spectrum for $N = 7$ atoms on a lattice of $L = 14$ sites (Hilbert space dimension 3432), revealing the absence of an energy gap.

The spectrum of many-body eigenstates can be measured by preparing the ground state with $N + 1$ atoms and extracting one atom, for example with a radiofrequency tuned close to resonance towards an initially empty internal state (see Fig. 3.5a). By measuring the position of outgoing atoms, one reconstructs the position-resolved spectral function

$$\rho(E, x) = \sum_i \delta(E - E_i) n_i(x),$$

obtained by summing excitations of energy E_i and density probability $n_i(x)$. The expected spectral function is shown in Fig. 3.5b. When the atom extraction is performed at 'zero' energy (with respect to the chemical potential μ), it occurs close to an end, as expected for a Majorana bound state. This observation would be the equivalent of the position-resolved measurements of in-gap states in solid-state systems [109].

A key asset of atomic gases is the ability to probe coherence between distant points [128, 129]. A central property of Majoranas is the long-range coherence between the two ends of the sample, which remains topologically protected from the environment. To reveal this feature, one could measure the momentum distribution of the atoms extracted at zero energy, by measuring their density distribution after free expansion [130, 97] (see Fig. 3.6). This protocol can be viewed as a double-slit interference between the two ends of the atomic wire. Remarkably, the interference phase can be expressed as

$$\phi = N\pi,$$

i.e. it only depends on the atom number parity $N \mod 2$. This dependence on such a non-local observable reveals a hidden topological order, defined over the atomic gas as a whole. This phase remains decoupled from perturbations acting locally, such as disorder, as long as the atom number parity is conserved.

The system discussed so far still lacks a degenerate subspace of protected Majorana excitations, the prerequisite for topologically protected quantum operations. Topological degeneracy would occur in a more complex setting, with a minimum of $2M$ defects with $M \geq 2$, each defect hosting a Majorana fermion. The associated Majorana bound states form a set of $M - 1$ qubits at zero energy, which can be manipulated by braiding operations. In practice, braiding cannot be performed in a single one-dimensional system. It requires extending the system to coupled one-dimensional systems [100] or two-dimensional geometry [102]. The complexity of the required experiment makes the description of a protocol out of the scope of this thesis.

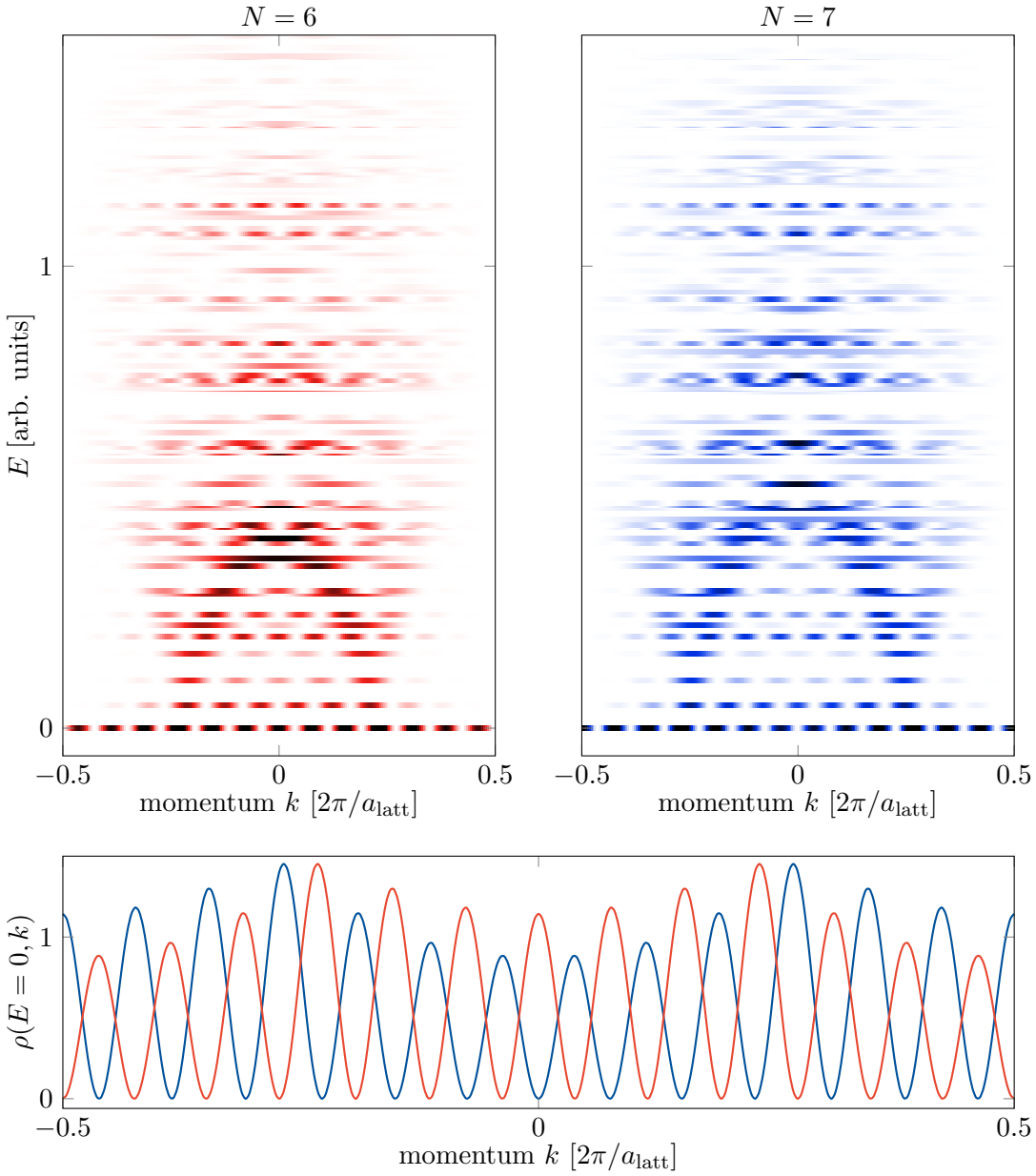

Figure 3.6: Momentum-resolved emission spectroscopy, for atom numbers $N = 6$ and 7. The spectral function $\rho(E, k)$ is plotted in red (blue) for $N = 6$ ($N = 7$). The lower panel shows the zero-energy spectral function, which forms a a double-slit interference pattern, as expected for a Majorana-like correlation between the two ends of the system. The parity of this interference pattern is determined by the atom number parity.

Conclusion

We have presented a series of projects on the experimental realization of quantum-enhanced sensing and the simulation of artificial gauge fields in ultracold dysprosium atoms.

The quantum sensing projects demonstrated the production of maximally sensitive N00N states via non-linear spin couplings. Future projects will aim at characterizing hidden entanglement in non-classical states and stabilizing the fragile N00N states using a maximal-order spin coupling. The developed techniques could be extended to study spinful interacting systems, providing a new path towards fractional quantum Hall states. They could also be applied to larger-spin systems, such as Rydberg atoms [131] or molecules [132], to further improve the sensing capabilities.

We presented two techniques to generate artificial gauge fields, in lattice atomic systems, and in dysprosium atomic gases based on a synthetic dimension encoded in the electronic spin. A grand challenge in the cold atom community is to combine gauge fields with interactions between atoms. The awaited strongly-interacting topological systems could reveal fascinating properties, such as non-abelian elementary excitations.

This manuscript only presents a selection of my research activity. During my postdoctoral stay in Munich, I performed experiments on lattice atomic gases. We studied gases in a mixture of two internal states at half filling, for which the low-energy dynamics is governed by superexchange between neighbouring spins. We demonstrated the control of XXZ-type superexchange [133], and studied resonating valence bond states in a four-site system [134].

Since my arrival at laboratoire Kastler Brossel as an associate professor, I co-supervised another ultracold atom experiment, together with Jean Dalibard and Jérôme Beugnon (principal investigator). This experiment works with samples of rubidium atoms, strongly confined along one spatial direction, allowing us to explore the physics of two-dimensional Bose gases. Despite the lack of long-range order, these systems exhibit a superfluid phase at low temperature. The superfluid transition occurs via the Berezinskii-Kosterlitz-Thouless mechanism, in which vortex/anti-vortex phase defects bind together below a critical temperature, such that the coherence decays with the distance very slowly. We studied several aspects of this transition, namely thermodynamic properties [135], sound propagation [136], first-order phase coherence [137] and particle bunching [138]. Among other projects, we also studied the universal non-equilibrium dynamics occurring when crossing a phase transition at finite speed, according to the Kibble-Zurek mechanism [139, 140, 141].

Bibliography

[1] L. Pezzè, A. Smerzi, M. K. Oberthaler, R. Schmied, and P. Treutlein. Quantum metrology with nonclassical states of atomic ensembles. *Rev. Mod. Phys.*, 90(3):035005, September 2018.

[2] C. L. Degen, F. Reinhard, and P. Cappellaro. Quantum sensing. *Reviews of modern physics*, 89(3):035002, 2017.

[3] T. Chalopin, C. Bouazza, A. Evrard, V. Makhalov, D. Dreon, J. Dalibard, L. A. Sidorenkov, and S. Nascimbene. Quantum-enhanced sensing using non-classical spin states of a highly magnetic atom. *Nature Communications*, 9(1):4955, November 2018.

[4] A. Evrard, V. Makhalov, T. Chalopin, L. A. Sidorenkov, J. Dalibard, R. Lopes, and S. Nascimbene. Enhanced Magnetic Sensitivity with Non-Gaussian Quantum Fluctuations. *Phys. Rev. Lett.*, 122(17):173601, May 2019.

[5] V. Makhalov, T. Satoor, A. Evrard, T. Chalopin, R. Lopes, and S. Nascimbene. Probing Quantum Criticality and Symmetry Breaking at the Microscopic Level. *Phys. Rev. Lett.*, 123(12):120601, September 2019.

[6] C. M. Caves. Quantum-mechanical noise in an interferometer. *Phys. Rev. D*, 23(8):1693–1708, April 1981.

[7] D. F. Walls. Squeezed states of light. *Nature*, 306(5939):141–146, November 1983.

[8] R. E. Slusher, L. W. Hollberg, B. Yurke, J. C. Mertz, and J. F. Valley. Observation of Squeezed States Generated by Four-Wave Mixing in an Optical Cavity. *Phys. Rev. Lett.*, 55(22):2409–2412, November 1985.

[9] L.-A. Wu, H. J. Kimble, J. L. Hall, and H. Wu. Generation of Squeezed States by Parametric Down Conversion. *Phys. Rev. Lett.*, 57(20):2520–2523, November 1986.

[10] L. Pezzé and A. Smerzi. Entanglement, Nonlinear Dynamics, and the Heisenberg Limit. *Phys. Rev. Lett.*, 102(10):100401, March 2009.

[11] E. Majorana. Atomi orientati in campo magnetico variabile. *Il Nuovo Cimento (1924-1942)*, 9(2):43–50, 1932.

[12] G. S. Agarwal. Relation between atomic coherent-state representation, state multipoles, and generalized phase-space distributions. *Phys. Rev. A*, 24(6):2889–2896, December 1981.

[13] M. Kitagawa and M. Ueda. Squeezed spin states. *Phys. Rev. A*, 47(6):5138–5143, June 1993.

[14] D. J. Wineland, J. J. Bollinger, W. M. Itano, F. L. Moore, and D. J. Heinzen. Spin squeezing and reduced quantum noise in spectroscopy. *Phys. Rev. A*, 46(11):R6797–R6800, December 1992.

[15] S. L. Braunstein and C. M. Caves. Statistical distance and the geometry of quantum states. *Phys. Rev. Lett.*, 72(22):3439–3443, May 1994.

[16] J. Estève, C. Gross, A. Weller, S. Giovanazzi, and M. K. Oberthaler. Squeezing and entanglement in a Bose–Einstein condensate. *Nature*, 455(7217):1216–1219, October 2008.

[17] C. Gross, T. Zibold, E. Nicklas, J. Estève, and M. K. Oberthaler. Nonlinear atom interferometer surpasses classical precision limit. *Nature*, 464(7292):1165–1169, April 2010.

[18] M. F. Riedel, P. Böhi, Y. Li, T. W. Hänsch, A. Sinatra, and P. Treutlein. Atom-chip-based generation of entanglement for quantum metrology. *Nature*, 464(7292):1170–1173, April 2010.

[19] R. Bücker, J. Grond, S. Manz, T. Berrada, T. Betz, C. Koller, U. Hohenester, T. Schumm, A. Perrin, and J. Schmiedmayer. Twin-atom beams. *Nature Physics*, 7(8):608–611, August 2011.

[20] B. Lücke, M. Scherer, J. Kruse, L. Pezzé, F. Deuretzbacher, P. Hyllus, O. Topic, J. Peise, W. Ertmer, J. Arlt, L. Santos, A. Smerzi, and C. Klempt. Twin Matter Waves for Interferometry Beyond the Classical Limit. *Science*, 334(6057):773–776, November 2011.

[21] H. Strobel, W. Muessel, D. Linnemann, T. Zibold, D. B. Hume, L. Pezzè, A. Smerzi, and M. K. Oberthaler. Fisher information and entanglement of non-Gaussian spin states. *Science*, 345(6195):424–427, 2014.

[22] S. P. Nolan, S. S. Szigeti, and S. A. Haine. Optimal and Robust Quantum Metrology Using Interaction-Based Readouts. *Phys. Rev. Lett.*, 119(19):193601, November 2017.

[23] P. Hyllus, W. Laskowski, R. Krischek, C. Schwemmer, W. Wieczorek, H. Weinfurter, L. Pezzé, and A. Smerzi. Fisher information and multiparticle entanglement. *Phys. Rev. A*, 85(2):022321, February 2012.

[24] G. Tóth. Multipartite entanglement and high-precision metrology. *Phys. Rev. A*, 85(2):022322, February 2012.

[25] A. Osterloh, L. Amico, G. Falci, and R. Fazio. Scaling of entanglement close to a quantum phase transition. *Nature*, 416(6881):608–610, April 2002.

[26] T. W. B. Kibble. Some implications of a cosmological phase transition. *Physics Reports*, 67(1):183–199, December 1980.

[27] W. H. Zurek. Cosmological experiments in superfluid helium? *Nature*, 317(6037):505–508, October 1985.

[28] H. J. Lipkin, N. Meshkov, and A. J. Glick. Validity of many-body approximation methods for a solvable model: (I). Exact solutions and perturbation theory. *Nucl. Phys.*, 62(2):188–198, February 1965.

[29] X.-Y. Luo, Y.-Q. Zou, L.-N. Wu, Q. Liu, M.-F. Han, M. K. Tey, and L. You. Deterministic entanglement generation from driving through quantum phase transitions. *Science*, 355(6325):620–623, February 2017.

[30] X. Wang and B. C. Sanders. Spin squeezing and pairwise entanglement for symmetric multiqubit states. *Phys. Rev. A*, 68(1):012101, July 2003.

[31] W. K. Wootters. Entanglement of Formation of an Arbitrary State of Two Qubits. *Phys. Rev. Lett.*, 80(10):2245–2248, March 1998.

[32] E. J. Mueller, T.-L. Ho, M. Ueda, and G. Baym. Fragmentation of Bose-Einstein condensates. *Phys. Rev. A*, 74(3):033612, September 2006.

[33] V. K. Kozin and O. Kyriienko. Quantum Time Crystals from Hamiltonians with Long-Range Interactions. *Phys. Rev. Lett.*, 123(21):210602, November 2019.

[34] Q. Niu. Viewpoint: A Quantum Constellation. *Physics*, 5, June 2012.

[35] F. D. M. Haldane. Fractional Quantization of the Hall Effect: A Hierarchy of Incompressible Quantum Fluid States. *Phys. Rev. Lett.*, 51(7):605–608, August 1983.

[36] B. Lian, T.-L. Ho, and H. Zhai. Searching for non-Abelian phases in the Bose-Einstein condensate of dysprosium. *Phys. Rev. A*, 85(5):051606, May 2012.

[37] X.-F. Zhou, C. Wu, G.-C. Guo, R. Wang, H. Pu, and Z.-W. Zhou. Synthetic Landau Levels and Spinor Vortex Matter on a Haldane Spherical Surface with a Magnetic Monopole. *Phys. Rev. Lett.*, 120(13):130402, March 2018.

[38] B. Lian and S. Zhang. Singlet Mott state simulating the bosonic Laughlin wave function. *Phys. Rev. B*, 89(4):041110, January 2014.

[39] K. W. Madison, F. Chevy, W. Wohlleben, and J. Dalibard. Vortex formation in a stirred Bose-Einstein condensate. *Physical Review Letters*, 84(5):806, 2000.

[40] J. R. Abo-Shaeer, C. Raman, J. M. Vogels, and W. Ketterle. Observation of vortex lattices in Bose-Einstein condensates. *Science*, 292(5516):476–479, 2001.

[41] N. R. Cooper. Rapidly rotating atomic gases. *Advances in Physics*, 57(6):539–616, 2008.

[42] V. Bretin, S. Stock, Y. Seurin, and J. Dalibard. Fast Rotation of a Bose-Einstein Condensate. *Physical Review Letters*, 92(5), February 2004.

[43] V. Schweikhard, I. Coddington, P. Engels, V. P. Mogendorff, and E. A. Cornell. Rapidly Rotating Bose-Einstein Condensates in and near the Lowest Landau Level. *Physical Review Letters*, 92(4), January 2004.

[44] J. Dalibard, F. Gerbier, G. Juzeliūnas, and P. Öhberg. *Colloquium* : Artificial gauge potentials for neutral atoms. *Reviews of Modern Physics*, 83(4):1523–1543, November 2011.

[45] M. V. Berry. Quantal phase factors accompanying adiabatic changes. In *Proceedings of the Royal Society of London A: Mathematical, Physical and Engineering Sciences*, volume 392, pages 45–57. The Royal Society, 1984.

[46] R. Dum and M. Olshanii. Gauge Structures in Atom-Laser Interaction: Bloch Oscillations in a Dark Lattice. *Phys. Rev. Lett.*, 76(11):1788–1791, March 1996.

[47] Y.-J. Lin, R. L. Compton, K. Jiménez-García, J. V. Porto, and I. B. Spielman. Synthetic magnetic fields for ultracold neutral atoms. *Nature*, 462(7273):628–632, December 2009.

[48] D. Jaksch, C. Bruder, J. I. Cirac, C. W. Gardiner, and P. Zoller. Cold Bosonic Atoms in Optical Lattices. *Phys. Rev. Lett.*, 81(15):3108–3111, October 1998.

[49] D. Jaksch and P. Zoller. Creation of effective magnetic fields in optical lattices: The Hofstadter butterfly for cold neutral atoms. *New J. Phys.*, 5:56–56, May 2003.

[50] M. Aidelsburger, M. Atala, S. Nascimbène, S. Trotzky, Y.-A. Chen, and I. Bloch. Experimental realization of strong effective magnetic fields in an optical lattice. *Physical review letters*, 107(25):255301, 2011.

[51] G. Jotzu, M. Messer, R. Desbuquois, M. Lebrat, T. Uehlinger, D. Greif, and T. Esslinger. Experimental realization of the topological Haldane model with ultracold fermions. *Nature*, 515(7526):237–240, November 2014.

[52] M. Aidelsburger, M. Lohse, C. Schweizer, M. Atala, J. T. Barreiro, S. Nascimbene, N. Cooper, I. Bloch, and N. Goldman. Measuring the Chern number of Hofstadter bands with ultracold bosonic atoms. *Nature Physics*, 11(2):162–166, 2015.

[53] A. Celi, P. Massignan, J. Ruseckas, N. Goldman, I. B. Spielman, G. Juzeliūnas, and M. Lewenstein. Synthetic Gauge Fields in Synthetic Dimensions. *Physical Review Letters*, 112(4), January 2014.

[54] M. Mancini, G. Pagano, G. Cappellini, L. Livi, M. Rider, J. Catani, C. Sias, P. Zoller, M. Inguscio, M. Dalmonte, and L. Fallani. Observation of chiral edge states with neutral fermions in synthetic Hall ribbons. *Science*, 349(6255):1510–1513, September 2015.

[55] B. K. Stuhl, H.-I. Lu, L. M. Aycock, D. Genkina, and I. B. Spielman. Visualizing edge states with an atomic Bose gas in the quantum Hall regime. *Science*, 349(6255):1514–1518, September 2015.

[56] T. Chalopin, T. Satoor, A. Evrard, V. Makhalov, J. Dalibard, R. Lopes, and S. Nascimbene. Probing chiral edge dynamics and bulk topology of a synthetic Hall system. *arXiv:2001.01664, to appear in Nature Phys.*, 2020.

[57] M. Aidelsburger, M. Atala, S. Nascimbène, S. Trotzky, Y.-A. Chen, and I. Bloch. Experimental realization of strong effective magnetic fields in optical superlattice potentials. *Applied Physics B*, 113(1):1–11, 2013.

[58] H. Lignier, C. Sias, D. Ciampini, Y. Singh, A. Zenesini, O. Morsch, and E. Arimondo. Dynamical Control of Matter-Wave Tunneling in Periodic Potentials. *Phys. Rev. Lett.*, 99(22):220403, November 2007.

[59] D. Jaksch and P. Zoller. Creation of effective magnetic fields in optical lattices: The Hofstadter butterfly for cold neutral atoms. *New J. Phys.*, 5:56–56, May 2003.

[60] A. R. Kolovsky. Creating artificial magnetic fields for cold atoms by photon-assisted tunneling. *EPL*, 93(2):20003, January 2011.

[61] P. G. Harper. Single Band Motion of Conduction Electrons in a Uniform Magnetic Field. *Proc. Phys. Soc. A*, 68(10):874–878, October 1955.

[62] D. R. Hofstadter. Energy levels and wave functions of Bloch electrons in rational and irrational magnetic fields. *Phys. Rev. B*, 14(6):2239–2249, September 1976.

[63] M. Bukov, L. D'Alessio, and A. Polkovnikov. Universal high-frequency behavior of periodically driven systems: From dynamical stabilization to Floquet engineering. *Advances in Physics*, 64(2):139–226, March 2015.

[64] A. Eckardt. Colloquium: Atomic quantum gases in periodically driven optical lattices. *Rev. Mod. Phys.*, 89(1):011004, March 2017.

[65] M. Weinberg, C. Ölschläger, C. Sträter, S. Prelle, A. Eckardt, K. Sengstock, and J. Simonet. Multiphoton interband excitations of quantum gases in driven optical lattices. *Phys. Rev. A*, 92(4):043621, October 2015.

[66] T. Bilitewski and N. R. Cooper. Scattering theory for Floquet-Bloch states. *Phys. Rev. A*, 91(3):033601, March 2015.

[67] M. Reitter, J. Näger, K. Wintersperger, C. Sträter, I. Bloch, A. Eckardt, and U. Schneider. Interaction Dependent Heating and Atom Loss in a Periodically Driven Optical Lattice. *Phys. Rev. Lett.*, 119(20):200402, November 2017.

[68] S. Lellouch, M. Bukov, E. Demler, and N. Goldman. Parametric Instability Rates in Periodically Driven Band Systems. *Phys. Rev. X*, 7(2):021015, May 2017.

[69] K. I. Seetharam, C.-E. Bardyn, N. H. Lindner, M. S. Rudner, and G. Refael. Controlled Population of Floquet-Bloch States via Coupling to Bose and Fermi Baths. *Phys. Rev. X*, 5(4):041050, December 2015.

[70] F. Gerbier and J. Dalibard. Gauge fields for ultracold atoms in optical superlattices. *New J. Phys.*, 12(3):033007, March 2010.

[71] M. Lu, N. Q. Burdick, S. H. Youn, and B. L. Lev. Strongly Dipolar Bose-Einstein Condensate of Dysprosium. *Physical Review Letters*, 107(19), October 2011.

[72] K. Aikawa, A. Frisch, M. Mark, S. Baier, A. Rietzler, R. Grimm, and F. Ferlaino. Bose-Einstein Condensation of Erbium. *Phys. Rev. Lett.*, 108(21):210401, May 2012.

[73] X. Cui, B. Lian, T.-L. Ho, B. L. Lev, and H. Zhai. Synthetic gauge field with highly magnetic lanthanide atoms. *Physical Review A*, 88(1), July 2013.

[74] B. I. Halperin. Quantized Hall conductance, current-carrying edge states, and the existence of extended states in a two-dimensional disordered potential. *Phys. Rev. B*, 25(4):2185–2190, February 1982.

[75] R. Bianco and R. Resta. Mapping topological order in coordinate space. *Phys. Rev. B*, 84(24):241106, December 2011.

[76] M. Barkeshli and X.-L. Qi. Topological Nematic States and Non-Abelian Lattice Dislocations. *Phys. Rev. X*, 2(3):031013, August 2012.

[77] Z. Liu, E. J. Bergholtz, H. Fan, and A. M. Läuchli. Fractional Chern Insulators in Topological Flat Bands with Higher Chern Number. *Phys. Rev. Lett.*, 109(18):186805, November 2012.

[78] Y.-F. Wang, H. Yao, C.-D. Gong, and D. N. Sheng. Fractional quantum Hall effect in topological flat bands with Chern number two. *Phys. Rev. B*, 86(20):201101, November 2012.

[79] J. P. Eisenstein, G. S. Boebinger, L. N. Pfeiffer, K. W. West, and S. He. New fractional quantum Hall state in double-layer two-dimensional electron systems. *Phys. Rev. Lett.*, 68(9):1383–1386, March 1992.

[80] L. Fu, C. L. Kane, and E. J. Mele. Topological Insulators in Three Dimensions. *Phys. Rev. Lett.*, 98(10):106803, March 2007.

[81] J. E. Moore and L. Balents. Topological invariants of time-reversal-invariant band structures. *Phys. Rev. B*, 75(12):121306, March 2007.

[82] M. Z. Hasan and C. L. Kane. *Colloquium* : Topological insulators. *Reviews of Modern Physics*, 82(4):3045–3067, November 2010.

[83] N. R. Cooper, J. Dalibard, and I. B. Spielman. Topological bands for ultracold atoms. *Rev. Mod. Phys.*, 91(1):015005, March 2019.

[84] B. Song, C. He, S. Niu, L. Zhang, Z. Ren, X.-J. Liu, and G.-B. Jo. Observation of nodal-line semimetal with ultracold fermions in an optical lattice. *Nat. Phys.*, 15(9):911–916, September 2019.

[85] Z.-Y. Wang, X.-C. Cheng, B.-Z. Wang, J.-Y. Zhang, Y.-H. Lu, C.-R. Yi, S. Niu, Y. Deng, X.-J. Liu, S. Chen, and J.-W. Pan. Realization of ideal Weyl semimetal band in ultracold quantum gas with 3D Spin-Orbit coupling. *arXiv:2004.02413 [cond-mat, physics:quant-ph]*, April 2020.

[86] B. Béri and N. R. Cooper. Z2 Topological Insulators in Ultracold Atomic Gases. *Phys. Rev. Lett.*, 107(14):145301, September 2011.

[87] L. Tarruell, D. Greif, T. Uehlinger, G. Jotzu, and T. Esslinger. Creating, moving and merging Dirac points with a Fermi gas in a tunable honeycomb lattice. *Nature*, 483(7389):302–305, March 2012.

[88] M. Aidelsburger, S. Nascimbene, and N. Goldman. Artificial gauge fields in materials and engineered systems. *Comptes Rendus Physique*, 19(6):394–432, September 2018.

[89] S. Barbarino, L. Taddia, D. Rossini, L. Mazza, and R. Fazio. Magnetic crystals and helical liquids in alkaline-earth fermionic gases. *Nat Commun*, 6(1):1–9, September 2015.

[90] R. B. Laughlin. Anomalous Quantum Hall Effect: An Incompressible Quantum Fluid with Fractionally Charged Excitations. *Phys. Rev. Lett.*, 50(18):1395–1398, May 1983.

[91] N. R. Cooper and N. K. Wilkin. Composite fermion description of rotating Bose-Einstein condensates. *Phys. Rev. B*, 60(24):R16279–R16282, December 1999.

[92] J. Esteve, J.-B. Trebbia, T. Schumm, A. Aspect, C. I. Westbrook, and I. Bouchoule. Observations of Density Fluctuations in an Elongated Bose Gas: Ideal Gas and Quasicondensate Regimes. *Phys. Rev. Lett.*, 96(13):130403, April 2006.

[93] N. Regnault and T. Jolicoeur. Quantum Hall Fractions in Rotating Bose-Einstein Condensates. *Phys. Rev. Lett.*, 91(3):030402, July 2003.

[94] N. Gemelke, X. Zhang, C.-L. Hung, and C. Chin. In situ observation of incompressible Mott-insulating domains in ultracold atomic gases. *Nature*, 460(7258):995–998, August 2009.

[95] B. Paredes, P. Fedichev, J. I. Cirac, and P. Zoller. $\frac12$-Anyons in Small Atomic Bose-Einstein Condensates. *Phys. Rev. Lett.*, 87(1):010402, June 2001.

[96] J. Zhang, J. Beugnon, and S. Nascimbene. Creating fractional quantum Hall states with atomic clusters using light-assisted insertion of angular momentum. *Physical Review A*, 94(4):043610, 2016.

[97] S. Nascimbene. Realizing one-dimensional topological superfluids with ultracold atomic gases. *Journal of Physics B: Atomic, Molecular and Optical Physics*, 46(13):134005, 2013.

[98] L. Mazza, S. Nascimbene, J. Dalibard, and C. Mora. Adiabatic continuity of Majorana zero modes from Kitaev's wire to ladders. *in preparation*, 2020.

[99] A. Y. Kitaev. Unpaired Majorana fermions in quantum wires. *Physics-Uspekhi*, 44(10S):131, 2001.

[100] J. Alicea, Y. Oreg, G. Refael, F. Von Oppen, and M. P. Fisher. Non-Abelian statistics and topological quantum information processing in 1D wire networks. *Nature Physics*, 7(5):412, 2011.

[101] N. Read and D. Green. Paired states of fermions in two dimensions with breaking of parity and time-reversal symmetries and the fractional quantum Hall effect. *Phys. Rev. B*, 61(15):10267–10297, April 2000.

[102] A. Y. Kitaev. Fault-tolerant quantum computation by anyons. *Annals of Physics*, 303(1):2–30, January 2003.

[103] C. Nayak, S. H. Simon, A. Stern, M. Freedman, and S. Das Sarma. Non-Abelian anyons and topological quantum computation. *Rev. Mod. Phys.*, 80(3):1083–1159, September 2008.

[104] G. Moore and N. Read. Nonabelions in the fractional quantum hall effect. *Nuclear Physics B*, 360(2):362–396, August 1991.

[105] C. Kallin. Chiral p-wave order in Sr2RuO4. *Rep. Prog. Phys.*, 75(4):042501, March 2012.

[106] A. Banerjee, C. A. Bridges, J.-Q. Yan, A. A. Aczel, L. Li, M. B. Stone, G. E. Granroth, M. D. Lumsden, Y. Yiu, J. Knolle, S. Bhattacharjee, D. L. Kovrizhin, R. Moessner, D. A. Tennant, D. G. Mandrus, and S. E. Nagler. Proximate Kitaev quantum spin liquid behaviour in a honeycomb magnet. *Nature Mater*, 15(7):733–740, July 2016.

[107] V. Mourik, K. Zuo, S. M. Frolov, S. Plissard, E. P. Bakkers, and L. P. Kouwenhoven. Signatures of Majorana fermions in hybrid superconductor-semiconductor nanowire devices. *Science*, 336(6084):1003–1007, 2012.

[108] L. P. Rokhinson, X. Liu, and J. K. Furdyna. The fractional a.c. Josephson effect in a semiconductor–superconductor nanowire as a signature of Majorana particles. *Nature Phys*, 8(11):795–799, November 2012.

[109] S. Nadj-Perge, I. K. Drozdov, J. Li, H. Chen, S. Jeon, J. Seo, A. H. MacDonald, B. A. Bernevig, and A. Yazdani. Observation of Majorana fermions in ferromagnetic atomic chains on a superconductor. *Science*, 346(6209):602–607, 2014.

[110] Y.-J. Lin, K. Jiménez-García, and I. B. Spielman. Spin–orbit-coupled Bose–Einstein condensates. *Nature*, 471(7336):83–86, March 2011.

[111] H. Zhai. Degenerate quantum gases with spin–orbit coupling: A review. *Rep. Prog. Phys.*, 78(2):026001, February 2015.

[112] L. W. Cheuk, A. T. Sommer, Z. Hadzibabic, T. Yefsah, W. S. Bakr, and M. W. Zwierlein. Spin-injection spectroscopy of a spin-orbit coupled Fermi gas. *Physical Review Letters*, 109(9):095302, 2012.

[113] P. Wang, Z.-Q. Yu, Z. Fu, J. Miao, L. Huang, S. Chai, H. Zhai, and J. Zhang. Spin-Orbit Coupled Degenerate Fermi Gases. *Phys. Rev. Lett.*, 109(9):095301, August 2012.

[114] N. Q. Burdick, Y. Tang, and B. L. Lev. Long-Lived Spin-Orbit-Coupled Degenerate Dipolar Fermi Gas. *Physical Review X*, 6(3):031022, 2016.

[115] C. Zhang, S. Tewari, R. M. Lutchyn, and S. D. Sarma. P x+ i p y Superfluid from s-Wave Interactions of Fermionic Cold Atoms. *Physical review letters*, 101(16):160401, 2008.

[116] K. Seo, C. Zhang, and S. Tewari. Thermodynamic signatures for topological phase transitions to Majorana and Weyl superfluids in ultracold Fermi gases. *Phys. Rev. A*, 87(6):063618, June 2013.

[117] M. Inguscio, W. Ketterle, and C. Salomon. *Ultra-Cold Fermi Gases*. IOS Press, April 2008.

[118] R. M. Lutchyn, E. P. a. M. Bakkers, L. P. Kouwenhoven, P. Krogstrup, C. M. Marcus, and Y. Oreg. Majorana zero modes in superconductor–semiconductor heterostructures. *Nat Rev Mater*, 3(5):52–68, May 2018.

[119] M. Cheng and H.-H. Tu. Majorana edge states in interacting two-chain ladders of fermions. *Phys. Rev. B*, 84(9):094503, September 2011.

[120] J. D. Sau, B. I. Halperin, K. Flensberg, and S. Das Sarma. Number conserving theory for topologically protected degeneracy in one-dimensional fermions. *Phys. Rev. B*, 84(14):144509, October 2011.

[121] C. V. Kraus, M. Dalmonte, M. A. Baranov, A. M. Läuchli, and P. Zoller. Majorana Edge States in Atomic Wires Coupled by Pair Hopping. *Phys. Rev. Lett.*, 111(17):173004, October 2013.

[122] L. Fidkowski, R. M. Lutchyn, C. Nayak, and M. P. A. Fisher. Majorana zero modes in one-dimensional quantum wires without long-ranged superconducting order. *Phys. Rev. B*, 84(19):195436, November 2011.

[123] P. Bonderson and C. Nayak. Quasi-topological phases of matter and topological protection. *Phys. Rev. B*, 87(19):195451, May 2013.

[124] A. Keselman and E. Berg. Gapless symmetry-protected topological phase of fermions in one dimension. *Phys. Rev. B*, 91(23):235309, June 2015.

[125] F. Iemini, L. Mazza, L. Fallani, P. Zoller, R. Fazio, and M. Dalmonte. Majorana quasiparticles in ultracold one-dimensional gases. In *Topological Phase Transitions and New Developments*, pages 97–113. WORLD SCIENTIFIC, April 2018.

[126] L. Jiang, T. Kitagawa, J. Alicea, A. Akhmerov, D. Pekker, G. Refael, J. I. Cirac, E. Demler, M. D. Lukin, and P. Zoller. Majorana fermions in equilibrium and in driven cold-atom quantum wires. *Physical review letters*, 106(22):220402, 2011.

[127] F. Iemini, L. Mazza, D. Rossini, R. Fazio, and S. Diehl. Localized Majorana-Like Modes in a Number-Conserving Setting: An Exactly Solvable Model. *Phys. Rev. Lett.*, 115(15):156402, October 2015.

[128] M. R. Andrews, C. G. Townsend, H.-J. Miesner, D. S. Durfee, D. M. Kurn, and W. Ketterle. Observation of Interference Between Two Bose Condensates. *Science*, 275(5300):637–641, January 1997.

[129] I. Bloch, T. W. Hänsch, and T. Esslinger. Measurement of the spatial coherence of a trapped Bose gas at the phase transition. *Nature*, 403(6766):166–170, January 2000.

[130] C. V. Kraus, S. Diehl, P. Zoller, and M. A. Baranov. Preparing and probing atomic Majorana fermions and topological order in optical lattices. *New J. Phys.*, 14(11):113036, November 2012.

[131] A. Facon, E.-K. Dietsche, D. Grosso, S. Haroche, J.-M. Raimond, M. Brune, and S. Gleyzes. A sensitive electrometer based on a Rydberg atom in a Schrödinger-cat state. *Nature*, 535(7611):262–265, July 2016.

[132] A. Frisch, M. Mark, K. Aikawa, S. Baier, R. Grimm, A. Petrov, S. Kotochigova, G. Quéméner, M. Lepers, O. Dulieu, and F. Ferlaino. Ultracold Dipolar Molecules Composed of Strongly Magnetic Atoms. *Phys. Rev. Lett.*, 115(20):203201, November 2015.

[133] Y.-A. Chen, S. Nascimbène, M. Aidelsburger, M. Atala, S. Trotzky, and I. Bloch. Controlling correlated tunneling and superexchange interactions with ac-driven optical lattices. *Physical review letters*, 107(21):210405, 2011.

[134] S. Nascimbène, Y.-A. Chen, M. Atala, M. Aidelsburger, S. Trotzky, B. Paredes, and I. Bloch. Experimental Realization of Plaquette Resonating Valence-Bond States with Ultracold Atoms in Optical Superlattices. *Physical Review Letters*, 108(20):205301, 2012.

[135] R. Desbuquois, T. Yefsah, L. Chomaz, C. Weitenberg, L. Corman, S. Nascimbène, and J. Dalibard. Determination of Scale-Invariant Equations of State without Fitting Parameters: Application to the Two-Dimensional Bose Gas Across the Berezinskii-Kosterlitz-Thouless Transition. *Physical review letters*, 113(2):020404, 2014.

[136] J. L. Ville, R. Saint-Jalm, É. Le Cerf, M. Aidelsburger, S. Nascimbène, J. Dalibard, and J. Beugnon. Sound Propagation in a Uniform Superfluid Two-Dimensional Bose Gas. *Phys. Rev. Lett.*, 121(14):145301, October 2018.

[137] In preparation.

[138] In preparation.

[139] L. Corman, L. Chomaz, T. Bienaimé, R. Desbuquois, C. Weitenberg, S. Nascimbene, J. Dalibard, and J. Beugnon. Quench-induced supercurrents in an annular Bose gas. *Physical review letters*, 113(13):135302, 2014.

[140] L. Chomaz, L. Corman, T. Bienaimé, R. Desbuquois, C. Weitenberg, S. Nascimbène, J. Beugnon, and J. Dalibard. Emergence of coherence via transverse condensation in a uniform quasi-two-dimensional Bose gas. *Nature communications*, 6, 2015.

[141] M. Aidelsburger, J. L. Ville, R. Saint-Jalm, S. Nascimbène, J. Dalibard, and J. Beugnon. Relaxation Dynamics in the Merging of N Independent Condensates. *Phys. Rev. Lett.*, 119(19):190403, November 2017.